PLOS Computational Biology

RESEARCH ARTICLE

Systematic computational assessment of atrial function impairment due to fibrotic remodeling in electromechanical properties

Åshild Telle[1,2], Ahmad Kassar[3], Nadia Chamoun[3], Romanos Haykal[3], Alejandro Gonzalo[4], Tori Hensley[3], Yaacoub Chahine[3], Oscar Flores[5], Juan C. del Álamo[1,3,6], Nazem Akoum[3], Christoph M. Augustin[7,8‡*], Patrick M. Boyle[1,2,3,6,9‡*]

1 Department of Bioengineering, University of Washington, Seattle, Washington, United States of America, **2** eScience Institute, University of Washington, Seattle, Washington, United States of America, **3** Division of Cardiology, Department of Medicine, University of Washington, Seattle, Washington, United States of America, **4** Department of Mechanical Engineering, University of Washington, Seattle, Washington, United States of America, **5** Department of Aerospace Engineering, Universidad Carlos III de Madrid, Leganés, Spain, **6** Center for Cardiovascular Biology, University of Washington, Seattle, Washington, United States of America, **7** Gottfried Schatz Research Center for Cell Signaling, Metabolism and Aging – Division of Medical Physics and Biophysics, Medical University of Graz, Graz, Austria, **8** BioTechMed-Graz, Graz, Austria, **9** Institute for Stem Cell and Regenerative Medicine, University of Washington, Seattle, Washington, United States of America

‡ Joint senior authors.
* christoph.augustin@medunigraz.at (CMA); pmjboyle@uw.edu (PMB)

OPEN ACCESS

Citation: Telle Å, Kassar A, Chamoun N, Haykal R, Gonzalo A, Hensley T, et al. (2025) Systematic computational assessment of atrial function impairment due to fibrotic remodeling in electromechanical properties. PLoS Comput Biol 21(12): e1013265. https://doi.org/10.1371/journal.pcbi.1013265

Editor: Anna Grosberg, UCI BME: University of California Irvine Department of Biomedical Engineering, UNITED STATES OF AMERICA

Received: June 23, 2025

Accepted: November 3, 2025

Published: December 5, 2025

Peer Review History: PLOS recognizes the benefits of transparency in the peer review process; therefore, we enable the publication of all of the content of peer review and author responses alongside final, published articles. The editorial history of this article is available here: https://doi.org/10.1371/journal.pcbi.1013265

Abstract

Cardiac fibrosis is a pathological condition associated with many cardiovascular diseases. Atrial fibrosis leads to reduced atrial function, resulting in diminished blood flow and an increased risk of stroke. This reduced function arises from altered myocardial electrophysiological and mechanical properties. Identifying the relative importance of these fibrosis-associated properties can reveal the most significant determinants of left atrial function impairment. In this study, we used a computational framework to investigate the relative importance of various fibrosis-associated properties. Our model, a 3D electromechanical framework coupled with a 0D circulatory model, incorporated patient-specific geometries and fibrosis distributions from clinical imaging data. Nine parameters related to fibrotic remodeling (conduction velocity, ion channel expression levels, cell- and tissue-scale contractility, and stiffness) were analyzed using two sensitivity analysis schemes: a one-factor-at-a-time setup, allowing for analysis of isolated effects, and a fractional factorial design, enabling examination of combined effects. As output, we tracked various metrics derived from model-predicted pressure-volume loops. Impairment of L-type calcium current (I_{CaL}) was most detrimental (up to 64% reduction in A-loop area of the left atrial pressure-volume relationship, quantifying work performed during atrial contraction). Conversely, reduced inward rectifier current (I_{K1}) led to improved atrial function (up to 27% increase in A-loop area). Detailed analysis of spatiotemporal distributions linked these effects to changes in intracellular calcium handling. Fractional factorial design

Data availability statement: The organ-level simulations were performed using proprietary software (CARPentry, Numericor; https://numericor.at), which cannot be made publicly available. The related openCARP software (https://opencarp.org/) is freely available for non-commercial use (https://opencarp.org). Supplementary Data for this study are published in a Dryad Repository (https://doi.org/10.5061/dryad.g79cnp62q), including: geometries used in the simulations, for all three patients and both fibrosis levels; the script used to calibrate CV values for all fibrotic combinations; all parameter combinations used in the two sensitivity analysis setups (OFAT and FFD); scripts used to perform all simulations with CARPentry, including both unloading and sensitivity analysis scripts; pressure and volume data from all cycles from all of the above-mentioned simulations for all three patients and both fibrosis levels. The code for performing the post-simulation sensitivity analysis is publicly available via Zenodo (https://doi.org/10.5281/zenodo.15693590), as is the code for material parameter estimation (https://doi.org/10.5281/zenodo.15693906).

Funding: This study was supported by the US National Institutes of Health grants R01-HL158667 (NA, JCA, CMA, PMB) and R01-HL160024 (JCA), and by the Austrian Science Fund grant 10.55776/P37063 (CMA). The funders did not play any role in the study design, data collection and analysis, decision to publish, or preparation of the manuscript.

Competing interests: The authors have declared that no competing interests exist.

analysis revealed that combination with other parameter changes blunted the impact of reduced I_{CaL} but amplified the impact of reduced I_{K1}. Future research focusing on I_{K1} and I_{CaL} could be highly significant for clinical and scientific advances. Modeling work can help evaluate left atrial function among larger patient cohorts, focusing on strain analysis. Our work could also be extended to spatiotemporal simulations of blood flow and thrombosis, shedding light onto the mechanisms underlying atriogenic stroke.

Author summary

Cardiac fibrosis is a process where healthy heart muscle is replaced with non-conductive, non-contractile tissue. This change disrupts how the heart beats and contracts. In the left atrium, fibrosis is linked to atrial fibrillation and a higher risk of stroke, the latter due to impaired pumping and altered blood flow. In this study, we used a detailed computer model of the heart, based on real patient-specific left atrial geometries and fibrosis patterns, to understand how different fibrosis-related changes affect atrial function. We tested nine features of the heart's electrical and mechanical behavior that are known to change during fibrosis, aiming to identify which ones have the most impact on the atrial function. We found that reducing the L-type calcium current — an important signal for muscle contraction — caused the greatest decrease in atrial performance. Surprisingly, reducing the inward rectifier potassium current improved it. These effects were tied to changes in calcium handling inside heart cells. Our findings highlight promising directions for future heart disease research and treatment.

1 Introduction

Cardiac fibrosis is prevalent in cardiovascular disease and contributes to left atrial (LA) dysfunction. LA fibrosis is strongly associated with atrial fibrillation (AF) and ischemic stroke [1–3]. Fibrotic remodeling encompasses a series of complex pathological events involving myocyte death, expansion of the extracellular matrix, and subcellular electromechanical changes [4,5]. These alterations reduces LA function, in which relative reduction can be quantified to support mechanistic insight and clinical risk stratification.

Fibrotic remodeling profoundly impacts myocardial electrophysiological (EP) and mechanical properties. Structural tissue-level changes (myocyte necrosis) lead to decreased conduction velocity (CV) [6] and reduced myocardial force generation. Subcellular remodeling reduces ion channel conductances [1,5], also leading to reduced contractility. LA fibrosis is furthermore linked to increased atrial stiffness [7], often attributed to up-regulated collagen crosslinking [8] and changes in collagen composition [9], likely combined with myocyte stiffening [10–12]. These changes affect the cardiac function, but our understanding of their relative contributions remains limited.

Computational modeling offers a powerful approach to elucidate the consequences of fibrosis-related alterations. By tuning parameters in physiologically informed models, one can predict consequences of specific pathological changes. Computational EP models of fibrotic LA have been used to study the connection between fibrosis and AF [13–16], revealing how altered CV and ion channel expression in fibrotic regions influence arrhythmia inducibility and spatial characteristics. Multi-physics, multi-scale modeling frameworks have been used to assess the impact of LA remodeling (including fibrosis) [17] and AF (without fibrosis) [18,19] on pressure-volume (PV) relationships. Hemodynamic effects of fibrotic remodeling have also been explored via computational fluid dynamics analyses [20,21]. All of these studies have shown utility in quantifying clinically relevant variables and enabling targeted investigations.

There are several approaches to make use of computational models to investigate individual impact of various parameters. One-factor-at-a-time (OFAT) analysis provides a systematic and straight-forward way to assess the isolated impact of each parameter [22,23], however, this does not account for combined or cooperative effects. Fractional factorial designs (FFD) setups offer a powerful method for reducing the parameter space by examining key combinations in a balanced and efficient manner [24,25]. It allows for investigating individual and interactive parameter effects, while minimizing the number of required experiments. FFDs and design of experiment protocols have previously been used to study parameter sensitivity in ionic EP models [26,27] and computational fluid dynamics analysis [28,29]. While FFD have been used only sparingly in cardiac computational modeling, the methodology hold potential for exploring large parameter spaces in detailed models of cardiac function [30]. To our knowledge, FFD has not yet been applied to multi-physics, organ-scale cardiac models.

This study combines computational modeling with OFAT and FFD analyses to disentangle the effects of various fibrosis-associated properties on atrial function. We performed simulations using three patient-specific LA geometries with corresponding fibrosis distributions, perturbing nine electromechanical parameters in fibrotic regions. First, we conducted an OFAT sensitivity analysis to assess the isolated effect of each parameter. Next, we explored spatiotemporal distributions of membrane potential, intracellular calcium, and active tension from the simulations in which these parameters were changed to elucidate the mechanisms driving their importance. To gain deeper understanding of combined interactive effects, we performed a more detailed sensitivity analysis using a 2^{9-5} FFD scheme. We then repeated both analyses with 50% synthetically elevated fibrosis in the same three geometries to assess the effect of an increasing fibrosis burden. As metrics, we tracked A-loop area, booster function, reservoir function, conduit function, and upstroke pressure difference during contraction, all derived from model-predicted PV loops. Sensitivity analyses based on these output values were used to identify the most influential parameters.

2 Methods

2.1 Ethics statement

The study was approved by the Institutional Review Board of the University of Washington (STUDY00015081). A written statement of consent was obtained from each patient.

2.2 Patient recruitment

We obtained three patient-specific LA geometries with corresponding spatial fibrosis and electroanatomical mapping (EAM) data. Participants were recruited at the University of Washington Medical Center, all of whom had AF and were scheduled for ablation. Patient demographics, LA clinical measurements, and modeling parameters are reported in Table 1.

Patients were directly recruited for this and subsequent studies, and not part of earlier cohorts. We included AF patients undergoing ablation procedures, with availability of LGE-MRI suitable for LA wall segmentation and fibrosis quantification, and indicated high-density EAM of the LA performed within a 1-month time-frame of the MRI scan. Exclusion criteria

Table 1. Patient-specific demographics, clinical measurements, and derived parameters.

	Patient 1	Patient 2	Patient 3
Age	81	63	70
Sex	F	M	F
LA end-diastolic volume (mL)	110.0	112.5	60.0
Body surface area (m^2)	1.98	2.33	1.73
LA volume index (mL/m^2)	55.5	48.3	34.7
LA emptying fraction (LAEF; %)	39.24	51.56	58.20
LA fibrosis burden (%)*	15.6	23.9	17.9
Synthetically increased fibrosis burden (%)*	23.4	35.85	26.85
LA wall thickness (min–max; mm)	1.4–2.4	2.3–3.0	1.6–2.4
Total LA activation time (ms)	82.0	56.0	116.8
CV longitudinal direction (CV_L; m/s)	1.1500	1.5730	0.835
CV transverse direction (CV_T; m/s)	0.5142	0.7035	0.373

*of main LA body and appendage (excluding pulmonary veins)

https://doi.org/10.1371/journal.pcbi.1013265.t001

were prior atrial ablation, prior cardiac surgery, contraindications to MRI or gadolinium contrast (e.g., device incompatibility, severe renal dysfunction, pregnancy, gadolinium sensitivity), and inability to obtain diagnostic-quality images due to arrhythmia or habitus constraints. The recruited patients included in this study all satisfied pre-specified data-quality requirements (diagnostic LGE-MRI enabling fibrosis segmentation and EAM with adequate LA surface coverage and point density).

2.3 Patient geometries and fibrosis distributions

LA geometries with corresponding fibrosis distributions were obtained from pre-ablation LGE-MRI images. MRI scans were taken at the end of atrial diastole (just prior to contraction). Segmentation, processing, and analysis of raw MRI scans were performed by Merisight (Marrek Inc., Salt Lake City, UT), as previously described [31] and applied [15,16,32]. Fibrosis burdens are reported in Table 1 and annotated in Fig 1. The geometries were represented as 3D triangulated surfaces with fibrosis distributions (LGE maps), which we extruded by 2 mm [33,34] outward to create volumetric geometries using CARPentry Studio (NumeriCor GmbH, Graz, Austria) [35]. We used a uniform thickness following literature rather than personalized values (with ranges reported in Table 1), as we did not have spatial thickness values co-registered with the geometries.

Fibrosis distributions in the volumetric geometries were interpolated from LGE maps. We used a priority-based protocol ensuring that the total fibrotic burdens matched those reported by Merisight. Volumetric mesh elements were sorted and given a priority value according to the interpolated normalized LGE value. Following this order, we assigned elements one by one as fibrotic until the volumetric fibrotic ratio matched the clinically reported fibrosis burden. Fibrotic tissue was assumed to be uniformly distributed from the epicardium to the endocardium, with no transmural variation. Fibrosis burden was calculated as a percentage of mesh elements excluding the pulmonary veins (i.e., only the LA body and appendage), for original LGE maps and our volumetric geometries alike. To explore the effects of extended fibrosis, we applied the same method but with a target fibrosis burden increased by 50% ($\times 1.5$). Effectively, this amounted to the identification of a lower cutoff value for normalized LGE in order for a element to be included. In practice, this generally resulted in expansion of fibrotic areas, although not necessarily uniformly since the approach was based on normalized intensity as opposed to geometric region growing. Fig 1A illustrates how fibrotic regions were mapped from LGE maps to volumetric geometries for both levels of fibrosis. Fig 1B displays the resulting volumetric geometries with corresponding fibrosis distributions.

Volumetric geometries were further augmented as needed for our electromechanical simulations. Pulmonary veins are clinically assumed passive post-ablation and were hence not included as LGE map distributions. However, they were

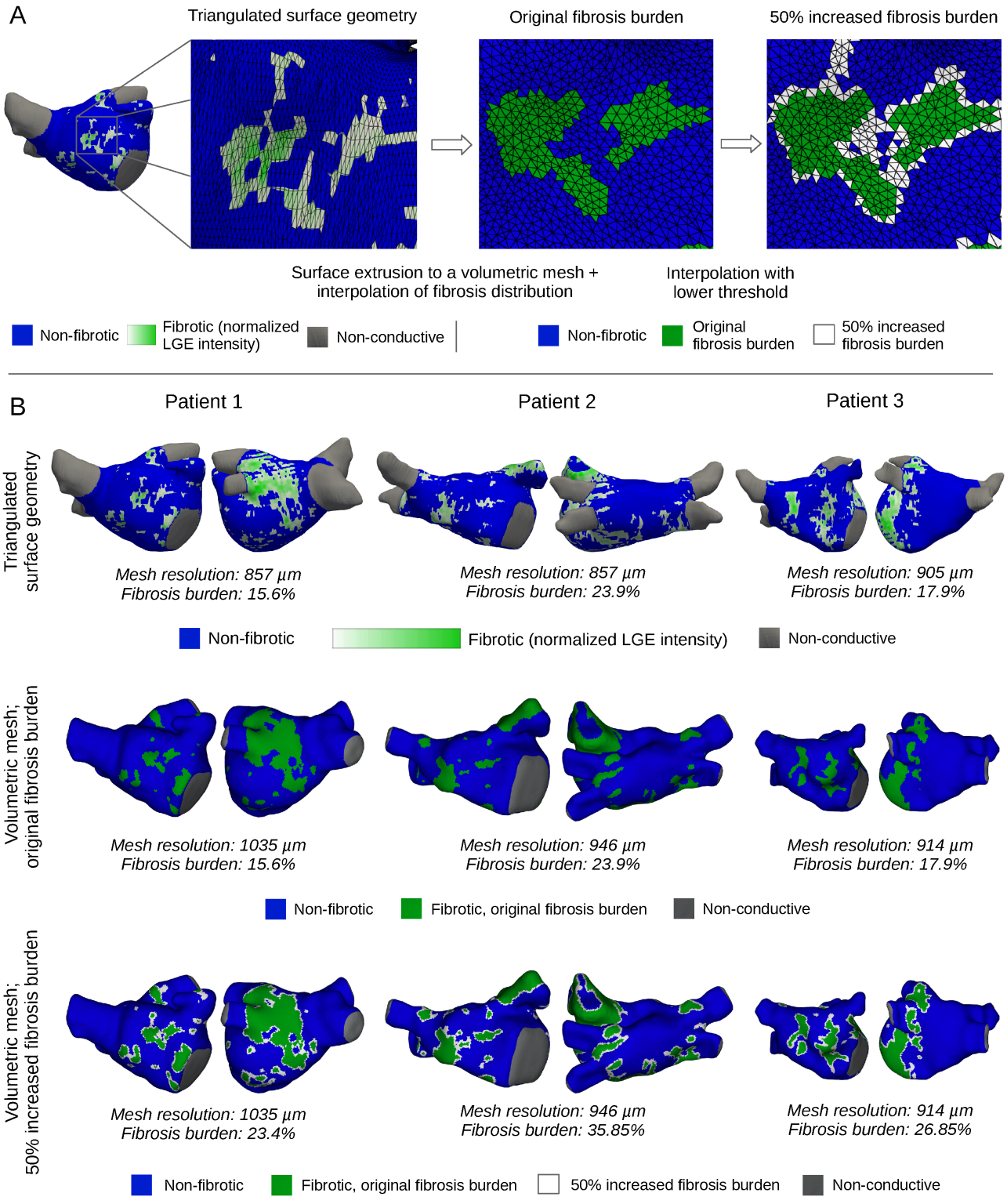

Fig 1. **Patient-specific geometries with fibrosis distributions.** (A) Workflow for mesh generation and fibrosis mapping: Starting with the original triangulated surfaces (left), we generated volumetric geometries. Fibrosis distributions were mapped via interpolation to preserve the original fibrosis burden (middle) and to reach a 50% synthetically elevated fibrosis burden (right). (B) Original shell geometries (top row), volumetric geometries with original fibrosis distributions (middle row), and volumetric geometries with increased fibrosis distributions (bottom row) for the three patient geometries considered in this study. Mesh resolutions (average tetrahedral edge length) and fibrotic burdens are included as annotations.

https://doi.org/10.1371/journal.pcbi.1013265.g001

included in our modeling geometries without corresponding fibrosis distributions. Artificial pulmonary vein caps and a mitral valve representation were added to the geometry to define boundary conditions and preserve anatomical orifice shape even under large deformations. Fiber direction maps (delineating the longitudinal myocyte directions) were generated for each geometry using a rule-based method defined by LA landmarks, similar to those described in previous publications [35,36]. The same fiber architecture was used in both baseline and fibrotic simulations. Volumetric meshes are publicly available in a Dryad Repository [37].

2.4 CV calibration and identification of earliest activation locations

EAM was performed and recorded for all patients during the ablation procedure, yielding LA activation maps in sinus rhythm. A CARTO (J&J MedTech) system was used to obtain the values during the procedure, and the open-source OpenEP package [38] was used to extract local activation maps post-procedure. EAM data was analyzed to identify each patient's earliest LA activation sites (first 5 ms) and total activation time.

Total activation times were used to personalize organ-scale CV values through an iterative inversion procedure. In this procedure, we fixed the anisotropy ratio for longitudinal CV (CV_L) versus transverse CV (CV_T) at $1:1/\sqrt{5}$ [14,15], limiting the optimization to a single varying parameter (CV_L). The optimization was performed by running EP simulations with our computational model, comparing the simulated to the recorded total activation time, and then adjusting the model's CV values accordingly. This process was repeated until the difference between model-predicted and recorded activation times was less than 1 ms.

Activation times, electrical stimulus locations, and resulting simulated activation are displayed in Fig 2, while resulting CV values are listed in Table 1. Reported values were representative for the whole tissue, without any adjustments for fibrotic regions. Additional details are provided as supplementary material, including detailed descriptions of the procedure (Sect A in S1 Text) and extended figures showing activation and electrical stimulus locations from multiple angles (Figs A-C in S1 Text).

2.5 Multi-scale, multi-physics LA modeling framework

To predict changes in atrial function under different conditions, we employed a multi-scale, multi-physics LA modeling framework. Electrical activation and mechanical contraction were modeled using a weakly coupled 3D electromechanical framework [21,39,40], with deformation strongly coupled to a 0D circulatory model [41]. Pulmonary veins were assumed to share the properties as non-fibrotic myocardium, exhibiting relative shortening within literature ranges [42].

Electrical activation was first modeled through a multiscale EP model, coupling cell- and tissue-scale dynamics. The cell-scale model was based on the human atrial action potential by Courtemanche et al. [43] with modifications according to Bayer et al. [44]. We simulated tissue-level electrical propagation using a reaction-eikonal model [45] with diffusion. Personalized CV values derived from EAM data (as described in Sect 2.4) were prescribed, for which baseline values are listed in Table 1. Pulmonary vein caps and the mitral valve were modeled as an in-excitable and non-conductive material.

The intracellular calcium distributions predicted by the EP framework was used as input to the biomechanical model. Active tension generation caused by intracellular calcium were computed using the cell-level contraction model by Land et al. [46,47]. Maximum active tension (T_a) was scaled with 50 kPa at baseline, calibrated to give approximately a 30% active LA emptying fraction (LAEF) [17,48–50]. Passive tension was modeled using a reduced Holzapfel-Ogden formulation with dispersion, with default material parameters $a = 2.92$ kPa, $b = 5.6$, $a_f = 11.84$ kPa, $b_f = 17.95$, and $\delta_f = 0.09$ [21,40]. Pulmonary caps and the mitral valve were modeled as a passive, stiff Demiray material [51], with material parameters $a = 10\,000$ kPa, $b = 5.6$. Both materials were modeled as nearly incompressible, with bulk modulus $\kappa = 650$ kPa [21].

To account for the impact of blood flow pressure and load from ventricular contraction, the 3D mechanical model of the LA was strongly coupled [41] with the 0D circulatory model CircAdapt [52,53]. Coupling between the 3D and 0D models was achieved by simulating 0D blood flow through the pulmonary veins into the LA and through the mitral valve

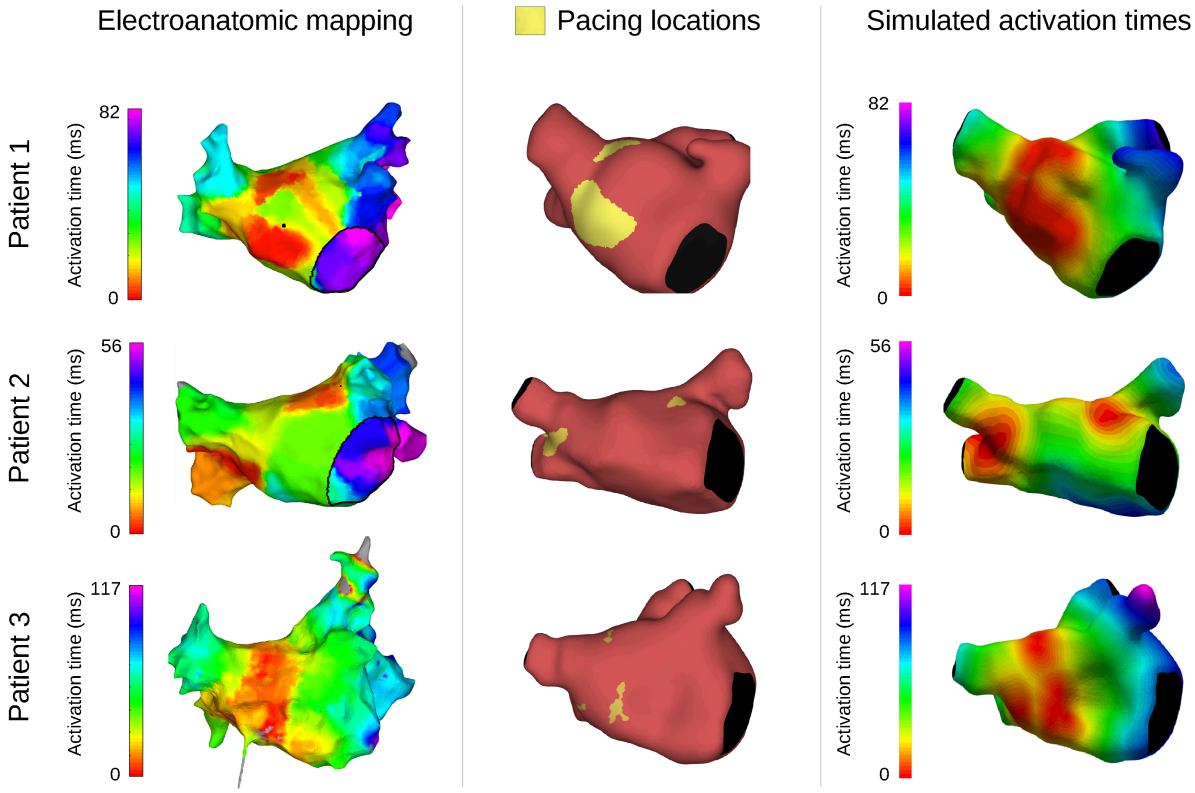

Fig 2. Electroanatomical mapping (EAM) activation time, electrical stimulation locations, and model activation times. Activation times estimated from EAM data (left), electrical stimulus locations corresponding to areas with the earliest activation times (first 5 ms, middle), and resulting activation times predicted by our EP model (right). All activation times are displayed relative to first LA activation.

https://doi.org/10.1371/journal.pcbi.1013265.g002

into the left ventricle, thereby modulating the pressure applied to the endocardial surface of the 3D LA model. Active tension generated in the 0D left ventricle was used to model atrioventricular plane displacement by applying a traction boundary condition on the mitral valve annulus of the 3D model. Additional mechanical constraints not captured in the 0D CircAdapt framework were imposed using Robin-type boundary conditions: spatially varying, normal spring boundary conditions were applied to the epicardial surface [54], while omnidirectional spring boundary conditions were imposed at the pulmonary vein inlets.

2.6 Simulation details

Simulations were performed using the software *Carpentry* (Numericor GmbH, Graz, Austria) [39], which is built on extensions of the open-source EP platform *openCARP* [55]. All simulations were carried out on Hyak, the University of Washington's high-performance computing cluster (on nodes with a Intel(R) Xeon(R) Gold 6230 CPU processor), in parallel using 40 processes. The steps taken to perform a full integrated simulation workflow are described below. All scripts used for the CARPentry simulations are publicly available [37].

We initially performed an unloading-reloading procedure to establish a physiologically accurate end-diastolic pressure configuration. This process ensured that the reinflated, pressurized geometry point-wise matched the initial mesh generated from image data. Specifically, we applied a backward displacement algorithm [56] to determine the unloaded reference configuration using a prescribed diastolic pressure of 10 mmHg [17,40], and reloaded this reference geometry with the same diastolic pressure.

To ensure physiologically reasonable initial states, we next performed electromechanical simulations at the cellular level using *openCARP*'s single-cell tool *bench*. These simulations were run for 50 cardiac cycles with a fine temporal resolution of 0.025 ms. Leveraging the substantially lower computational cost of cell-level simulations compared to full organ-scale models, this approach allowed efficient approximation of steady-state conditions. The resulting cellular states were then used to initialize the full organ-scale simulations.

Organ-scale simulations were then performed for ten cardiac cycles with the full 3D framework. The ten cycles were simulated to reach a convergent state (convergence plots for baseline simulations displayed in Fig 3; in the 10th cycle there was less than 2% difference for both pressure and volume), balanced with a reasonable running time (16–20 hours per simulation).

The simulated end-diastolic volumes were slightly higher than the corresponding clinical measurements (Table 1; Fig 3, middle row). This was expected given that the volume computations in the simulations were performed on a closed atrial cavity that included the pulmonary vein remnants, see Fig 1. Specifically, the simulations yielded end-diastolic LA volumes of 124.2 mL, 130.9 mL, and 63.4 mL, compared to clinically measured volumes of 110.0 mL, 112.5 mL, and 60.0 mL. This systematic offset was consistent with the modeling approach and demonstrated an overall agreement between simulated and clinical data.

For each cycle, activation was initiated by applying an electrical stimulus in earliest activation regions, determined by EAM data (as described in Sect 2.4). The remaining myocardial tissue was then activated through the propagation of the electrical signal, leading to atrial contraction as simulated by our modeling pipeline. We imposed a 1 Hz frequency to mimic sinus rhythm. Time steps were discretized at 0.025 ms for the EP model and 0.5 ms for the coupled biomechanical-0D circulatory model. The PV loops predicted by the final cycle simulated were used for our subsequent analysis.

2.7 Parameter changes in fibrotic regions

In our investigation of consequences of various fibrosis-related properties, we focused on five EP parameters (CV values and ion channel currents) and four mechanical parameters (contractile and passive properties), summarized in Table 2. Each parameter was re-scaled in the fibrotic regions by the corresponding factor (second column). Baseline or fibrotic parameter values were assigned in various combinations following the sensitivity analyses described in Sect 2.8. An overview of all parameter absolute values across all combinations is publicly available [37].

For CV values, we independently explored reductions in the longitudinal and transverse directions. CV_L was scaled a factor of 0.657, based on values reported by Macheret et al. [16]. For CV_T, we used a scaling factor of 0.520 (relative to baseline CV_T values), corresponding to a fibrotic anisotropy ratio of $1:1/\sqrt{8}$. This imposed higher anisotropy compared to the non-fibrotic ratio $1:1/\sqrt{5}$, consistent with previous studies [14,15].

Changes in ionic currents were imposed by scaling the inward rectifier potassium (I_{K1}), L-type calcium (I_{CaL}), and fast sodium (I_{Na}) currents by factors of 0.5, 0.5, and 0.6, respectively [14,15,57–59]. These changes in ionic current levels

Table 2. Fibrotic remodeling parameter changes.

Parameter	Scaling factor(s)	Notes	References
CV longitudinal direction (CV_L)	0.657		[16]
CV transverse direction (CV_T)	0.520	Anisotropy ratio $1:1/\sqrt{8}$	[14,15]
Inward rectifier potassium current (I_{K1})	0.5	Also alters CV values	[14,15,57–59]
L-type calcium current (I_{CaL})	0.5	Also alters CV values	[14,15,57–59]
Fast sodium current (I_{Na})	0.6	Also alters CV values	[14,15,57–59]
Myofilament binding rate (μ)	0.5		[60,61]
Active tension scaling factor (T_a)	0.5		[21,62]
Increased longitudinal stiffness (ST_L)	$a \times 0.963$, $a_f \times 2.293$	2 × load upon 5% stretch longitudinal direction	[7,62]
Increased transverse stiffness (ST_T)	$a \times 2.157$, $a_f \times 0.675$	2 × load upon 5% stretch transverse direction	[7,62]
$\Rightarrow ST_L$ *and* ST_T *in combination*	$a \times 2.009$, $a_f \times 2.000$		

https://doi.org/10.1371/journal.pcbi.1013265.t002

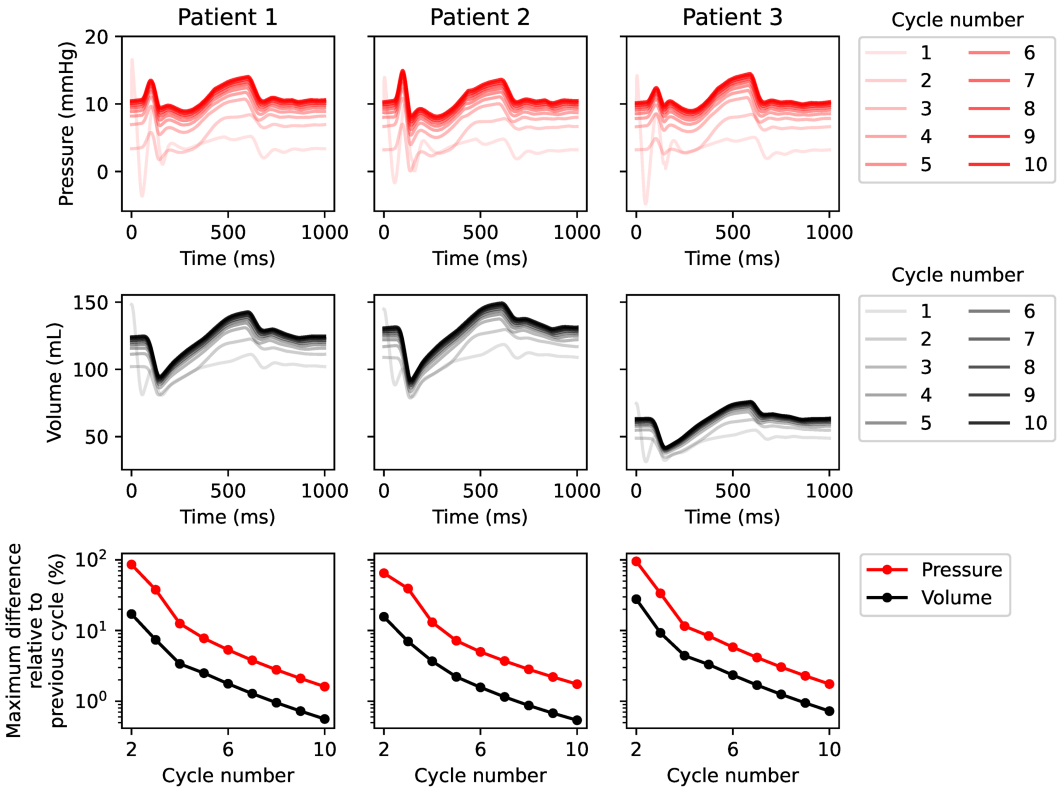

Fig 3. Convergence plots for baseline simulations. LA pressure (top), volume (middle) over time for ten cardiac cycles, and maximum differences in respective values between subsequent cardiac cycles, normalized by the maximum value of the last cycle (bottom). Values shown are shown for Patient 1–3, at baseline.

https://doi.org/10.1371/journal.pcbi.1013265.g003

are known to alter CV values locally [63,64]. In traditional tissue- and organ-scale EP models, these alterations would be captured indirectly through changes in membrane potential. However, the reaction-eikonal formulation we used in our study does not inherently account for the direct effects of ionic current changes. CV values are here prescribed and not emergent properties of the underlying cell- and tissue-scale EP dynamics. To prescribe accurate CV values, we ran supplement simulations using OpenCarp's *tuneCV* functionality [65]. These simulations were performed considering a simplified 1D rod to predict appropriate CV scaling factors for all combinations of ionic scaling factors. These are described in Sect B of S1 Text, and the corresponding scripts are published [37]. The resulting CV values for all possible parameter combinations, including in combination with reduced CV_L and CV_T, are listed in Table A in S1 Text.

For contractile properties, we considered the active tension scaling factor (T_a) and the myofilament binding rate (μ). Modifications to T_a affect the magnitude of the active transient. We applied a fibrotic scaling factor of 50% for T_a [21,62] (relative to the baseline value of 50 kPa). The myofilament binding rate depends on the ratio of α and β myosin isoforms. This ratio shifts to a higher proportion of β myosins in AF [60,61], resulting in a slower contraction rate. We here imposed a fibrotic scaling factor of 50% (relative to the baseline value $\mu = 9$ [47]).

To account for increased myocardial stiffness, we altered passive material parameters imposing changes in longitudinal (ST_L) and transverse (ST_T) stiffness. Specifically, we altered parameters a, which affects isotropic stiffness, and a_f, which alters additional fiber direction stiffness. To consider stiffness independently for each direction, we performed virtual stretch experiments. Through these experiments we estimated values of a and a_f needed to achieve a two-fold change

in the load (i.e., force per area) in one direction while keeping the load in the other direction unchanged. In these experiments, we stretched a tissue block (a unit cube) by 5% in either direction while tracking the corresponding load values, following the setup described in a previous publication [66]. Through an iterative procedure, we then stretched the tissue block, compared new load values with previous values, then altered the values of a and a_f. We repeated the process until the load value doubled upon stretching in one direction while remaining unchanged in the other direction (within 1% precision). For the combined effect, having both ST_L and ST_T set to fibrotic levels, we found values of a and a_f such that load values doubled when stretched 5% in either direction. Resulting a and a_f values are listed in Table 2. Unloading-reloading procedures were performed for each geometry at both levels of fibrosis and for all four stiffness configurations (without any changes, with increased ST_L, with increased ST_T, and both combined). The code for material parameter estimation is publicly available on Zenodo [67].

2.8 Sensitivity analysis – experimental setup

We investigated the impact of the nine identified fibrosis-associated parameters using two approaches. First, we used an OFAT analysis to analyze each parameter's isolated effect. Next, we used a FFD analysis to evaluate combined effects. We employed a 2^{9-5} design [68] as displayed in Table 3, resulting in 32 distinct parameter combinations. In this setup, B denotes the baseline factor level, while F represents the fibrosis-associated factor level, incorporating the relevant scaling factors (listed in Table 2). The code for performing the post-simulation sensitivity analysis is publicly available on Zenodo [69], and the pressure and volume data from all simulations are available on Dryad [37].

2.9 Metrics reported

For all simulations, we reported five PV-loop-based metrics capturing different aspects of atrial function. These included A-loop area [70–72], booster function, reservoir function, conduit function [73,74], and upstroke pressure difference during contraction. The metrics are defined in the equations given below. Here, LAV_{preA} and LAP_{preA} refer to the LA volume and pressure at the time point for initial electrical stimulus (LA pre-systolic/LA end-diastolic volume), LAV_{min} and LAV_{max} refer to the minimal (LA end-systole) and maximal volumes, and LAP_{maxA} refers to the maximal pressure during the A-loop (i.e., maximum value of booster phase pressure). We performed statistical analysis on values normalized by the corresponding baseline values for the same patient.

The five metrics considered were:

1. A-loop area (work performed during the active contraction), calculated by Gauss's area formula:

$$A = \frac{1}{2}\sum_{i=1}^{n} p_i(v_{i+1} - v_{i-1}) = \frac{1}{2}\left(\sum_{i=1}^{n} p_i v_{i+1} - \sum_{i=1}^{n} p_{i-1} v_i\right) \quad (1)$$

Table 3. FFD setup; B = baseline value; F = fibrotic value.

	Combination number																															
	1	2	3	4	5	6	7	8	9	10	11	12	13	14	15	16	17	18	19	20	21	22	23	24	25	26	27	28	29	30	31	32
CV_L	B	F	B	F	B	F	B	F	B	F	B	F	B	F	B	F	B	F	B	F	B	F	B	F	B	F	B	F	B	F	B	F
CV_T	B	B	F	F	B	B	F	F	B	B	F	F	B	B	F	F	B	B	F	F	B	B	F	F	B	B	F	F	B	B	F	F
I_{K1}	B	B	B	B	F	F	F	F	B	B	B	B	F	F	F	F	B	B	B	B	F	F	F	F	B	B	B	B	F	F	F	F
I_{CaL}	B	B	B	B	B	B	B	B	F	F	F	F	F	F	F	F	B	B	B	B	B	B	B	B	F	F	F	F	F	F	F	F
I_{Na}	B	B	B	B	B	B	B	B	B	B	B	B	B	B	B	B	F	F	F	F	F	F	F	F	F	F	F	F	F	F	F	F
μ	F	F	B	B	B	B	F	F	B	B	F	F	F	F	B	B	B	B	F	F	F	F	B	B	F	F	B	B	B	B	F	F
T_a	F	B	F	B	B	F	B	F	B	F	B	F	F	B	F	B	B	F	B	F	F	B	F	B	F	B	F	B	B	F	B	F
ST_L	F	B	B	F	F	B	B	F	B	F	F	B	B	F	F	B	B	F	F	B	B	F	F	B	F	B	B	F	F	B	B	F
ST_T	F	B	B	F	B	F	F	B	F	B	B	F	B	F	F	B	B	F	F	B	F	B	B	F	B	F	F	B	F	B	B	F

https://doi.org/10.1371/journal.pcbi.1013265.t003

where p and v correspond to A-loop volume and pressure values.

2. Booster function (LA pumping function, active contraction volume change):

$$\frac{LAV_{preA} - LAV_{min}}{LAV_{preA}} \tag{2}$$

3. Reservoir function (elastic ability to stretch and recoil, passive stretching):

$$\frac{LAV_{max} - LAV_{min}}{LAV_{min}} \tag{3}$$

4. Conduit function (passive transfer of blood to the LV):

$$\frac{LAV_{max} - LAV_{preA}}{LAV_{max}} \tag{4}$$

5. Upstroke pressure difference (LA pumping function, active contraction pressure change):

$$\frac{LAP_{maxA} - LAP_{preA}}{LAP_{preA}} \tag{5}$$

2.10 Spatiotemporal analysis

We examined spatiotemporal distributions of electromechanical simulations to better understand the effects of the parameters identified as most influential. Specifically, we compared the baseline simulation, those in which I_{CaL} and I_{K1} were impaired (from the OFAT analysis), and FFD Combination 32, in which all parameters were set to fibrotic levels. For conciseness, we refer to this combination as "Fully fibrotic" throughout the paper. We compared spatiotemporal distributions of membrane voltage, intracellular calcium, active tension, and fiber direction strain. This analysis was limited to the original fibrosis burden, with Patient 1 as a representative example.

2.11 FFD analysis

To analyze the FFD main effect (isolated impact of a single parameter, but in combination with other parameter changes), we compared the baseline (B) and fibrotic (F) groups. For a given parameter, the B group included all combinations in which that parameter was set to baseline value, while the F group includes combinations where it was set to the fibrotic value (as defined in Table 2). Other parameters were set to either baseline or fibrotic levels according to the design. Statistical comparisons between the two groups were performed using Student's t-test (with group-wise distributions found to be normal, as assessed by an Anderson-Darling test). The analysis was conducted and annotated using the software Statannotations [75].

To characterize FFD interaction effects (confounded effects with other parameters), the subdivision was extended to pairwise combinations. This resulted in four groups for each parameter pair (x_i, x_j) – all combinations of baseline/fibrotic levels (B_iB_j, F_iB_j, B_iF_j, and F_iF_j). We defined an interaction coefficient as a cross-product between these:

$$I_{i,j} = \arcsin\left(\frac{[F_iB_j, F_iF_j] \times [B_iB_j, B_iF_j]}{\|[F_iB_j, F_iF_j]\| \, \|[B_iB_j, B_iF_j]\|}\right). \tag{6}$$

The coefficient relates the angle between two lines in an interaction plot. It is symmetric, meaning $I_{i,j} = I_{j,i}$. Positive values indicate a *synergistic effect*, where the impact of having both variables at fibrotic levels leads to a greater reduction in

atrial function than the sum of the effects of individual factors. Negative values indicate *mitigating effect*, where the impact of having both variables at fibrotic levels leads to a smaller reduction in atrial function compared to the sum of the effects of individual factors.

3 Results

In this section, we present findings from individual patient-specific simulations, using Patient 1 as a representative example, and statistical analysis of aggregated data. We begin by presenting an overview of the simulation pipeline, PV loops with derived metrics for all three patients, followed by OFAT analysis results. We next present results from the spatiotemporal analysis focusing on parameter changes emerging as most important from the OFAT analysis, followed by FFD analysis results. Finally, we examine the impact of increased fibrosis. Unless otherwise noted, the results are representative of all three patients and reflect the original fibrosis burden.

3.1 Electromechanical simulations and PV loop-based metrics

Our modeling pipeline is demonstrated in Fig 4, for Patient 1 at baseline (no fibrotic changes). The model-predicted pressure and volume transients were extracted, resulting in characteristic LA PV loops. The A-loop was larger than the V-loop in area, indicating higher changes in volume and pressure. Prior to atrial contraction (when we were close to an equilibrium between atrial and ventricular pressure), we observed small oscillations in both volume and pressure, also are visible in the lower part of the V-loop.

Baseline PV loops for all three patients are displayed in Fig 5, with derived metric values annotated. Patient 1 had the smallest booster and reservoir function. Patient 2 had the largest A-loop area and upstroke pressure difference, and the lowest conduit function (although only marginally lower than Patient 1). Patient 3 had the smallest A-loop area and upstroke pressure difference, but the highest booster, conduit, and reservoir function. No patient consistently showed higher metric values than the others.

Based on volumetric measurements at different stages, we also computed model-predicted LAEF for comparison with clinical values (reported in Table 1). Total LAEFs at baseline were 33.70% for Patient 1, 38.13% for Patient 2, and 37.52%; consistently lower than corresponding clinical estimates. Simulation-predicted active LAEFs were 23.99%, 29.37%, and 33.97%, while passive LAEFs were 12.78%, 12.16%, and 16.61% for Patients 1–3.

3.2 OFAT analysis predicted fibrosis-associated decreases in I_{CaL} and I_{K1} as main determinants of LA function

Results of our OFAT analysis are presented in Fig 6, highlighting the isolated effect of each parameter change. Fig 6A shows the impact on PV loops using Patient 1 as a representative example. Impaired I_{K1} enlarged the A-loop, while impaired I_{CaL} (substantially) and reduced T_a (marginally) decreased it. Increased stiffness (i.e., higher ST_F and ST_T) shifted the PV loop, increasing volume while preserving pressure and loop shape. Modifying CV_L, CV_T, I_{Na}, or μ did not noticeably alter PV loop size or shape.

Relative changes in PV-loop-derived metrics are plotted in Fig 6B. There were consistent trends across all three patients, with comparable magnitude changes. The largest changes were observed for Patient 2 (who had the highest fibrosis burden). A-loop area was the most sensitive metric (at maximum leading to a 74% reduction for impaired I_{CaL} for Patient 2).

Fig 6C displays output metrics and fibrosis-associated input parameters averaged across all three patients. Reducing I_{CaL} substantially decreased atrial function (with the largest decrease in A-loop area, 64%), while reducing I_{K1} increased function (with the largest increase in A-loop area, 20%). Reducing T_a also had an effect (17% decrease in A-loop area). The impact of the other factors was otherwise modest. Notably, reduced CV and increased stiffness did not alter any metric by more than 5%.

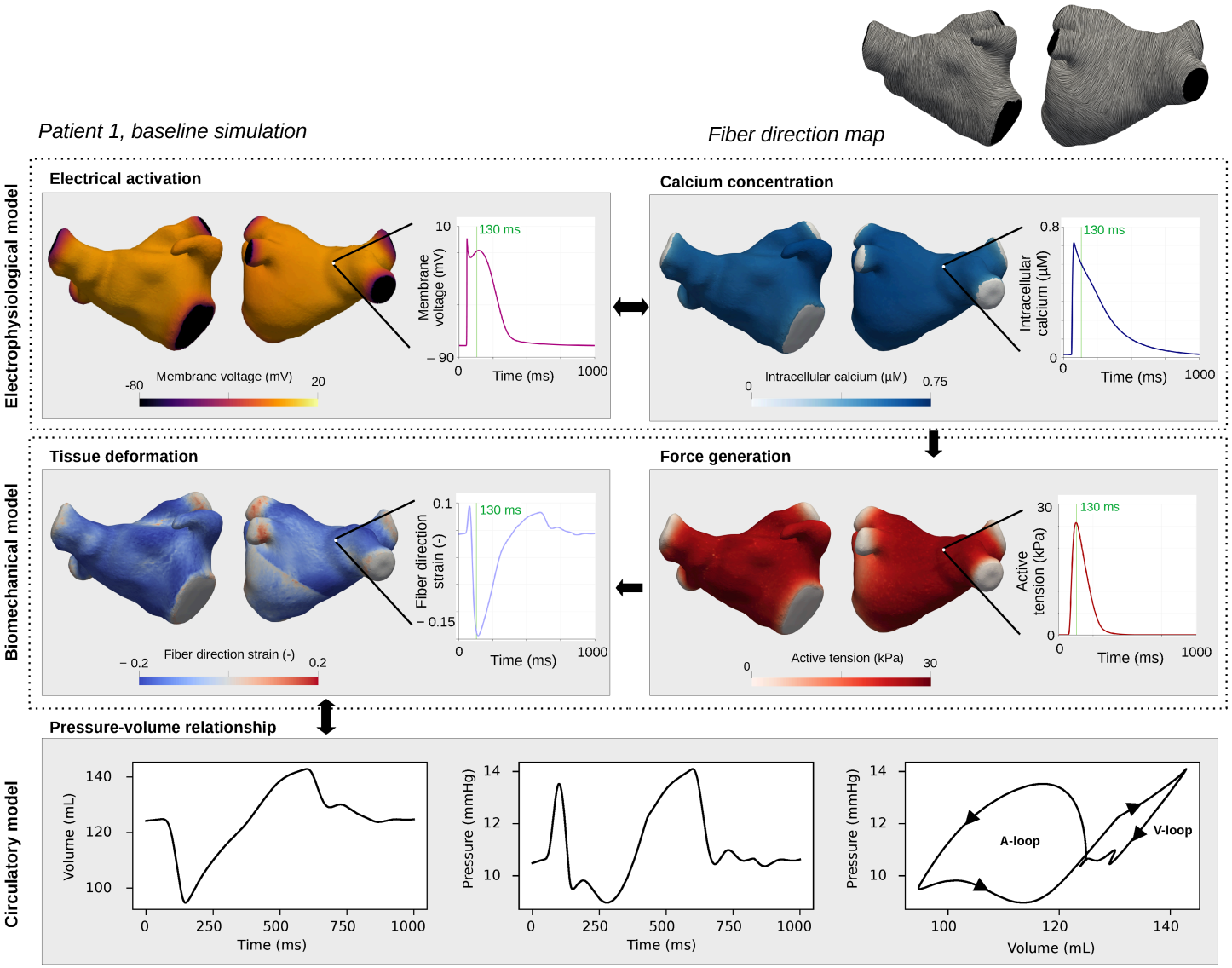

Fig 4. Model pipeline: EP, biomechanical, and circulatory models. Electrical propagation, including the release of intracellular calcium, was modeled with the EP model. The intracellular calcium resulted in active tension generation in our biomechanical model, leading to tissue deformation. Tissue deformation was strongly coupled to the 0D circulatory model, from which we extracted LA volume and pressure transients. 3D maps (left) show the spatial distribution of model outputs at the 130 ms time point, and transient plots (right) display values over time at a representative node. Output data are shown for Patient 1, baseline simulation (no fibrotic changes). Movies displaying spatiotemporal distributions for all three patients are included as supplementary material (S1 Movie, S2 Movie, and S3 Movie).

https://doi.org/10.1371/journal.pcbi.1013265.g004

3.3 Impact of impaired I_{CaL} and I_{K1} was related to changes in intracellular calcium transient amplitude

Motivated by the results from the OFAT analysis, we next compared key spatiotemporal distributions across baseline, impaired I_{CaL}, impaired I_{K1}, and fully fibrotic simulations. Spatiotemporal distributions for all three patients under these conditions are also included as supplementary material (S1 Movie, S2 Movie, and S3 Movie).

Fig 7 shows membrane potential, intracellular calcium, and active tension for each condition, using Patient 1 as a representative example. In the simulation with impaired I_{CaL}, membrane potential was lower in fibrotic areas, while

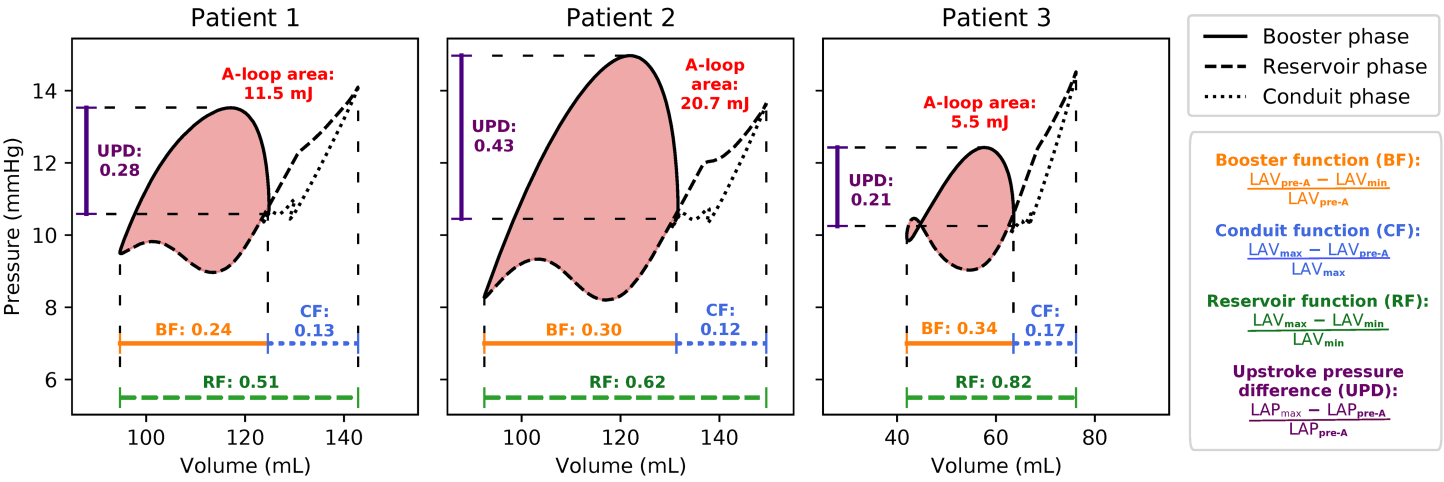

Fig 5. PV loops and derived metrics. PV loops from baseline simulations for all three patients, with derived metrics annotated: A-loop area (i.e., stroke work in mJ), booster function (BF), conduit function (CF), reservoir function (RF), and upstroke pressure difference (UPD).

https://doi.org/10.1371/journal.pcbi.1013265.g005

intracellular calcium was intermediate, and active tension was close to zero. A dispersive effect was also observed for calcium and active tension, lower in non-fibrotic areas than in the baseline simulation (compare, e.g., the lower left region). In contrast, impaired I_{K1} abolished the differences between fibrotic and non-fibrotic regions producing a slight increase in intracellular calcium and a marked rise in active tension relative to baseline (see also transients in Fig 8). The fully fibrotic simulation exhibited pronounced heterogeneity in the intracellular calcium distribution, with near-zero values centrally and intermediate closer to non-fibrotic areas. Active tension was close to zero in all fibrotic regions, but higher in non-fibrotic areas compared to the impaired I_{CaL} simulation.

Fig 8 shows membrane potential, intracellular calcium, and active tension transients for three representative locations in Patient 1's geometry. The fibrotic site and its immediate vicinity (Points A and B) exhibited an elevated resting membrane potential (approximately 5 mV increase) and a prolonged action potential duration (approximately 75 ms longer) in the impaired I_{K1} and fully fibrotic simulations. No differences were observed at the distant site (Point C) for the membrane potential. Intracellular calcium transient amplitude was reduced for the impaired I_{CaL} simulation and slightly increased for the impaired I_{K1} simulation across all points, with gradual effect from Point A to Point B to Point C. In the fully fibrotic simulation, intracellular calcium was close to zero in Point A (see also corresponding spatial plots in Fig 7, bottom middle) while being reduced in Point B (14% decrease in amplitude, relative to baseline) and Point C (7% decrease). These calcium variations were magnified in active tension, with attenuated responses at lower calcium levels and enhanced responses at higher calcium levels. For the fully fibrotic simulation, active tension was zero in Point A, while reduced in Point B (44% decrease, relative to baseline) and Point C (19% decrease).

In Fig 9A, we show LA deformation comparing baseline to the other configurations. Deformation is displayed at the time of minimum volume (i.e., LA systole, see Fig 9B, top subplot). In the impaired I_{CaL} simulation (top row), the LA remained more dilated, indicating reduced contraction. Conversely, for impaired I_{K1} (middle row), the deformed geometry was slightly more contracted than the baseline simulation. The fully fibrotic simulation (bottom row) also resulted in a less contracted geometry.

Fig 9B displays corresponding differences in volume and pressure over time. The systolic volumes were similar between impaired I_{CaL} and fully fibrotic simulations, while the fully fibrotic simulation exhibited a larger maximum volume. Pressure displayed highest differences during contraction, with the impaired I_{CaL} and fully fibrotic simulations having less variation than the baseline and impaired I_{K1} ones. The PV loop in the fully fibrotic simulation was shifted in

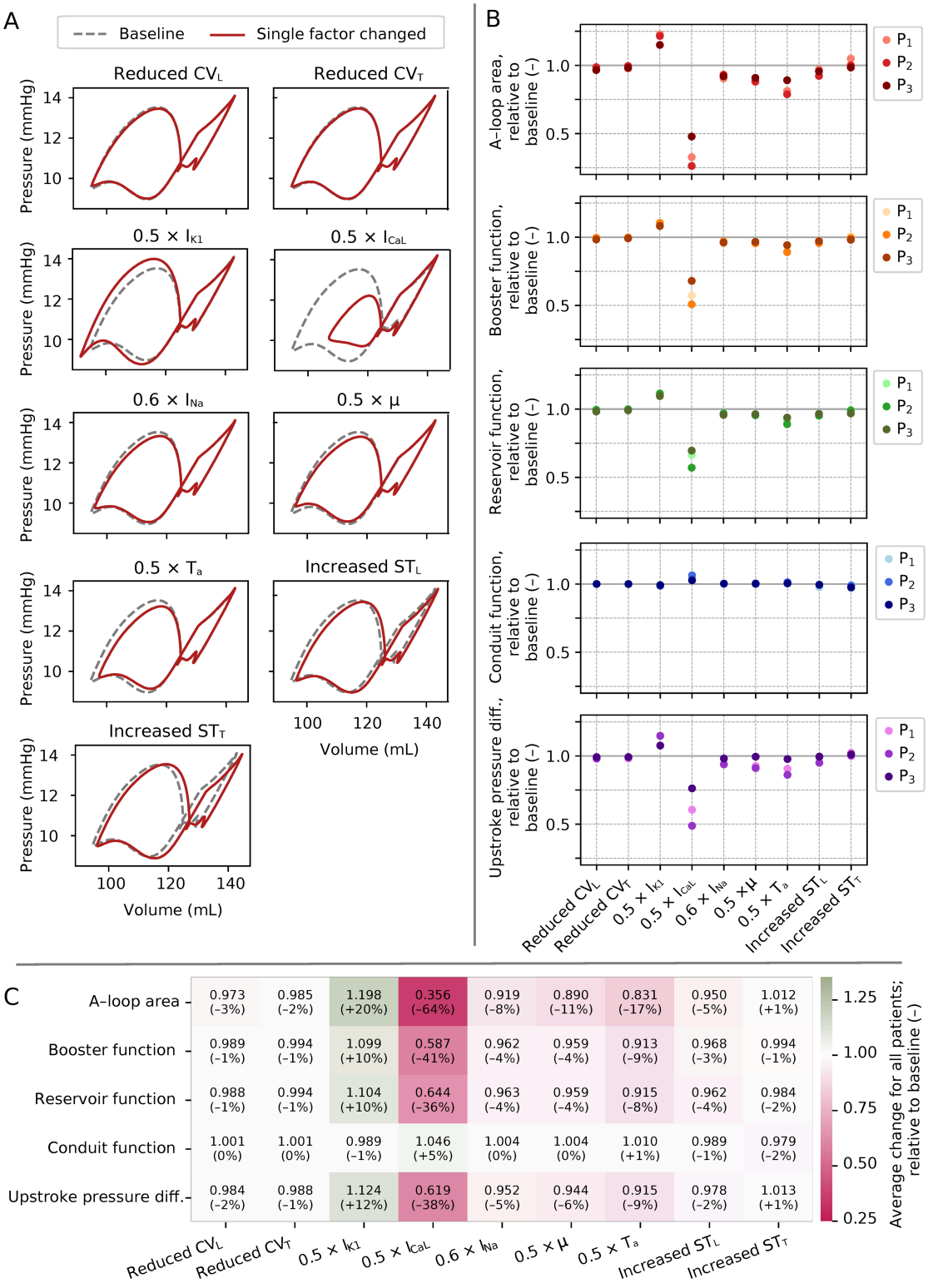

Fig 6. Results from OFAT analysis, original fibrosis burden. (A) PV loops with one parameter changed (red) compared to baseline (gray, dotted), for Patient 1. (B) Impact of each parameter on A-loop area, booster function, conduit function, reservoir function, and upstroke pressure difference for Patients 1–3 (P_1–P_3). Values reported relative to baseline. (C) Average change (across all three patients) in each metric for each parameter, with implied percent-wise changes in parentheses.

https://doi.org/10.1371/journal.pcbi.1013265.g006

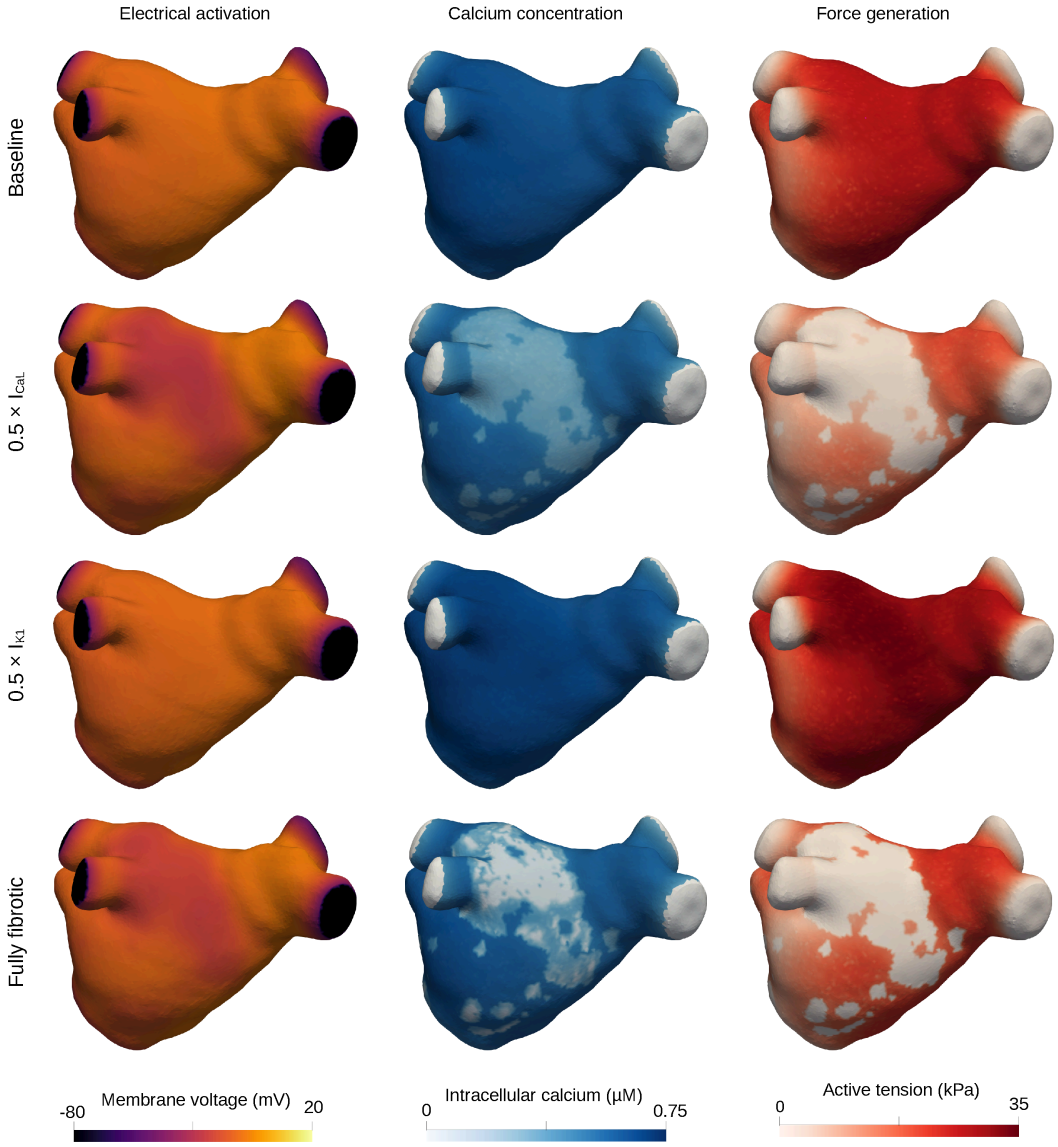

Fig 7. Spatial distributions of membrane potential, intracellular calcium, and active tension; baseline, impaired I_{CaL}, impaired I_{K1}, and fully fibrotic simulations. Spatial distributions of membrane potential (left), intracellular calcium (middle), and active tension (right) at time step 130 ms for baseline (top), impaired I_{CaL} (second row), impaired I_{K1} (third row), and fully fibrotic (bottom row) simulations for Patient 1. See also corresponding point-wise plots displayed in Fig 8 and movies attached as supplementary material (S1 Movie, S2 Movie, and S3 Movie).

https://doi.org/10.1371/journal.pcbi.1013265.g007

volume compared to all the other cases, and the A-loop was smaller than baseline and impaired I_{K1} but larger than in the I_{CaL} simulation.

3.4 FFD analysis predicted I_{CaL}, I_{K1}, longitudinal, and transverse stiffness as significant factors

To gain deeper understanding of the interactions between model parameters, we next performed a detailed FFD analysis. The PV loops obtained from simulations for all FFD combinations are shown in Fig 10, in which most combinations reduced the A-loop. Patient-averaged metric values for all combinations are included in Fig D in S1 Text, and further described in Sect C in S1 Text. For Combination 32 (fully fibrotic), the relative change in A-loop area was 0.474

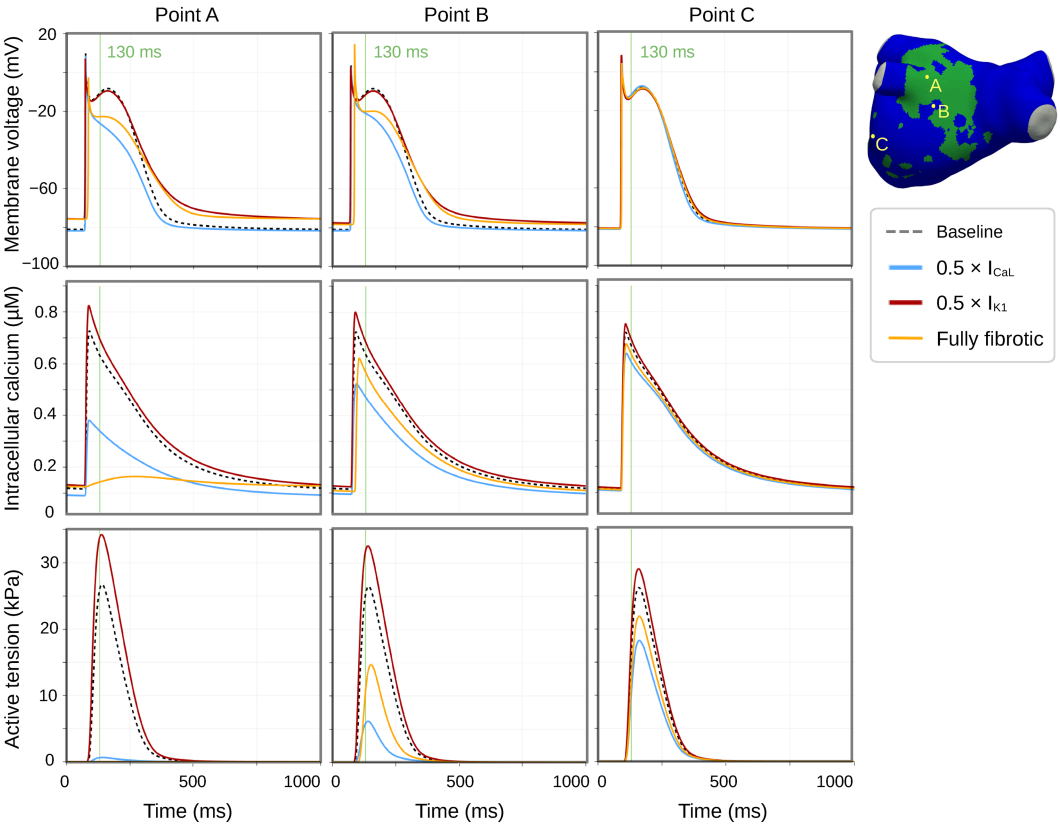

Fig 8. Membrane potential, intracellular calcium, and active tension in selected points; baseline, impaired I_{CaL}, impaired I_{K1}, and fully fibrotic simulations. Membrane voltage, intracellular calcium, and active tension transients for three representative points (Point A – inside the fibrotic area, Point B – close to the fibrotic area, and Point C – away from the fibrotic area), Patient 1. Note that active tension for Point A in the fully fibrotic simulation was zero everywhere (not visible in the plot). See also corresponding spatial plots displayed in Fig 8.

https://doi.org/10.1371/journal.pcbi.1013265.g008

(i.e., −53%), in booster function 0.673 (−33%), in reservoir function 0.695 (−30%), in conduit function 1.0 (no change), and in upstroke pressure difference 0.721 (−28%).

Main effect plots for all patients and combinations are displayed in Fig 11A, with the relative change of each factor shown in Fig 11B. Reduced I_{CaL} and I_{K1} had a statistically significant impact on four of five metrics when comparing B and F groups, the impact in line with the OFAT analysis. The effect of impaired I_{CaL} was slightly attenuated (e.g., 54% reduction in A-loop area vs. 64% reduction in the OFAT analysis), whereas the impact of I_{K1} impairment was amplified (e.g., 27% increase in A-loop area vs. 20% increase in the OFAT analysis). Consistent with our OFAT analysis, changes in CV and stiffness had a modest impact (less than 2%).

Increasing stiffness had a statistically significant, albeit modest impact on conduit function, with decreases of 1% and 2% for increases in longitudinal and transverse stiffness, respectively. The impact was small in magnitude relative to the effects observed for the other metrics, with little variation (all standard deviations less than 0.03, and all observations were within the range [0.95,1.06]).

Interaction effects presented in Fig 12 were generally small. All interaction coefficients (Fig 12A) were less than 0.1 radians, and interaction lines nearly parallel (Fig 12B–12C). Most combinations were found to be mitigating (having negative interaction values, see again Fig 12A). For A-loop area, booster function, reservoir function, and upstroke

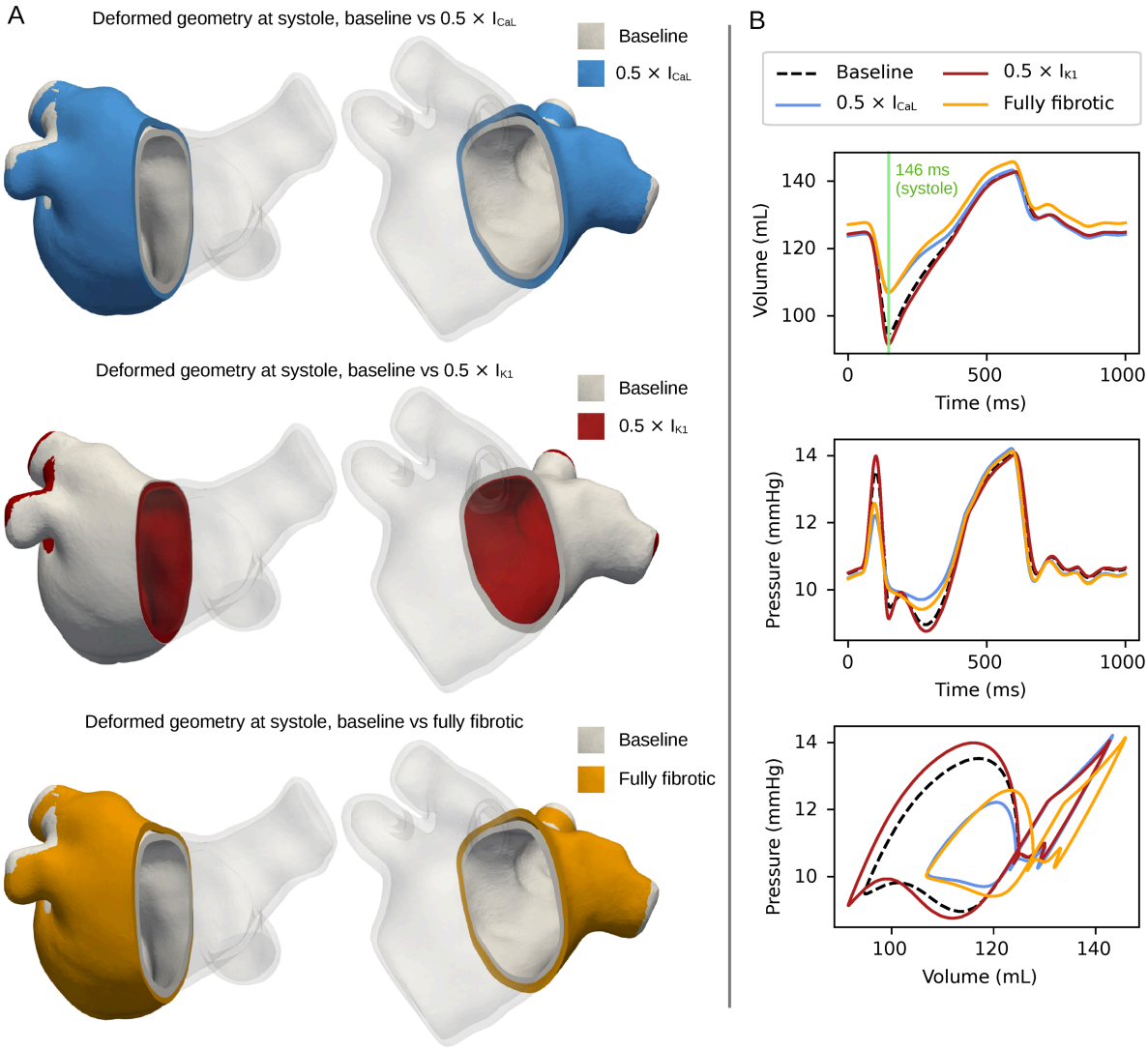

Fig 9. Geometry deformation and changes in volume and pressure – comparison of baseline with impaired I_{CaL}, impaired I_{K1}, and fully fibrotic simulations. (A) Deformed geometries for impaired I_{CaL} vs. baseline (top), impaired I_{K1} vs. baseline (middle), and fully fibrotic vs. baseline (bottom) simulations, Patient 1. Deformation is displayed from two angles, with partial transparency. (B) Volume over time, pressure over time, and PV loops for the same simulations.

https://doi.org/10.1371/journal.pcbi.1013265.g009

pressure difference, the greatest mitigating effect consistently was for reduced CV_T combined with increased ST_T. There was also a mitigating effect for I_{CaL} combined with I_{K1} – strongest for A-loop area, followed by booster function.

3.5 Increased fibrosis led to moderate further reduction in LA function

Results of our analysis with a 50% synthetically elevated fibrosis burden are presented in Fig 13. Increased fibrosis burden led to a further reduction across all metrics in the OFAT analysis (Fig 13A), however, the decrease was moderate. Factors identified as statistically significant for FFD main effect subject to original fibrosis burden remained significant with elevated fibrosis (Fig 13B). Considering average values (Fig 13C), the largest increase in absolute effect was observed

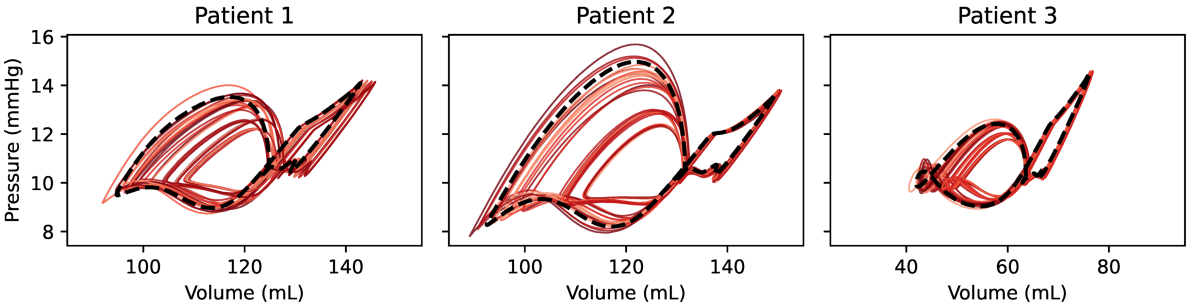

Fig 10. PV loops for all FFD combinations, original fibrosis burden. PV loops from all FFD combinations, for all three patients. Baseline PV loops are displayed with a bolder black dotted line, while the thinner red traces correspond to FFD combinations, as listed in Table 2.

https://doi.org/10.1371/journal.pcbi.1013265.g010

for impaired I_{CaL}. For A-loop area, we observed a 74% decrease with elevated fibrosis (compared to 64% with the original fibrosis burden) in the OFAT analysis, and a 62% decrease (compared to 54%) in the FFD analysis. Patient-averaged metric values for all FFD combinations are included in Fig E in S1 Text, and described in Sect C in S1 Text. For Combination 32 (fully fibrotic), the relative change in A-loop area was 0.366 (i.e., −63%), booster function 0.584 (−42%), reservoir function 0.622 (−38%), conduit function 0.995 (+0.5%, more precisely +0.462 rounded down to 0 in the heatmap), and upstroke pressure difference 0.657 (−34%).

In Fig 14 we display how absolute values of all metrics vary between no fibrosis, original fibrosis, and increased fibrosis burden, considering the fully fibrotic simulations. The decrease in all but the conduit function was steeper going from no fibrosis to original fibrosis burden compared to going from original to elevated fibrosis burden. Patient-specific trends correlated well between A-loop area and upstroke pressure difference, and between booster function and reservoir function, while conduit function differed from all other metrics.

4 Discussion

4.1 Impact of fibrotic-associated parameter changes on the atrial function

In the present study, we combined a multi-scale, multiphysics modeling framework with patient-specific LA geometries and fibrosis maps to investigate the impact of fibrotic remodeling. We investigated the influence of nine electromechanical parameters altered in fibrosis, and assessed LA function using five volume- and pressure-based metrics. We found these metrics to be sensitive to variations in I_{CaL} and I_{K1}, with opposite effects, while stiffness exerted a small but statistically significant impact on conduit function. Spatiotemporal analysis revealed that changes in intracellular calcium transient amplitude had pronounced effects on active tension impairment, reflecting the nonlinear relationship between these variables. In simulations with impaired I_{K1}, we observed an elevated membrane potential and an increase in intracellular calcium transient amplitude (Fig 8), leading to enhanced active tension and improved LA function. This effect mitigated the impairing impact of fibrosis from other factors.

The effect of I_{CaL} on atrial function is consistent with its central role in regulating intracellular calcium release [76], driving cardiac contraction [77]. Atrial function remains impaired after sinus rhythm restoration in AF patients, primarily due to reduced I_{CaL} [78]. Less intuitive was the improved atrial function following impaired I_{K1}. Experimental studies show that increased intracellular calcium reduces I_{K1} [79–81], making it plausible that impaired I_{K1} raises intracellular calcium. To our knowledge, this is the first study delineating the impact of individual fibrosis-associated changes on atrial function through electromechanical simulations on patient-specific geometries. However, our results align with those of Hurtado et al. [82], who found L-type calcium channel conductance, followed by potassium delayed rectifier conductances, to be the most sensitive parameters in ventricular electromechanical model representations. They also found L-type calcium channel

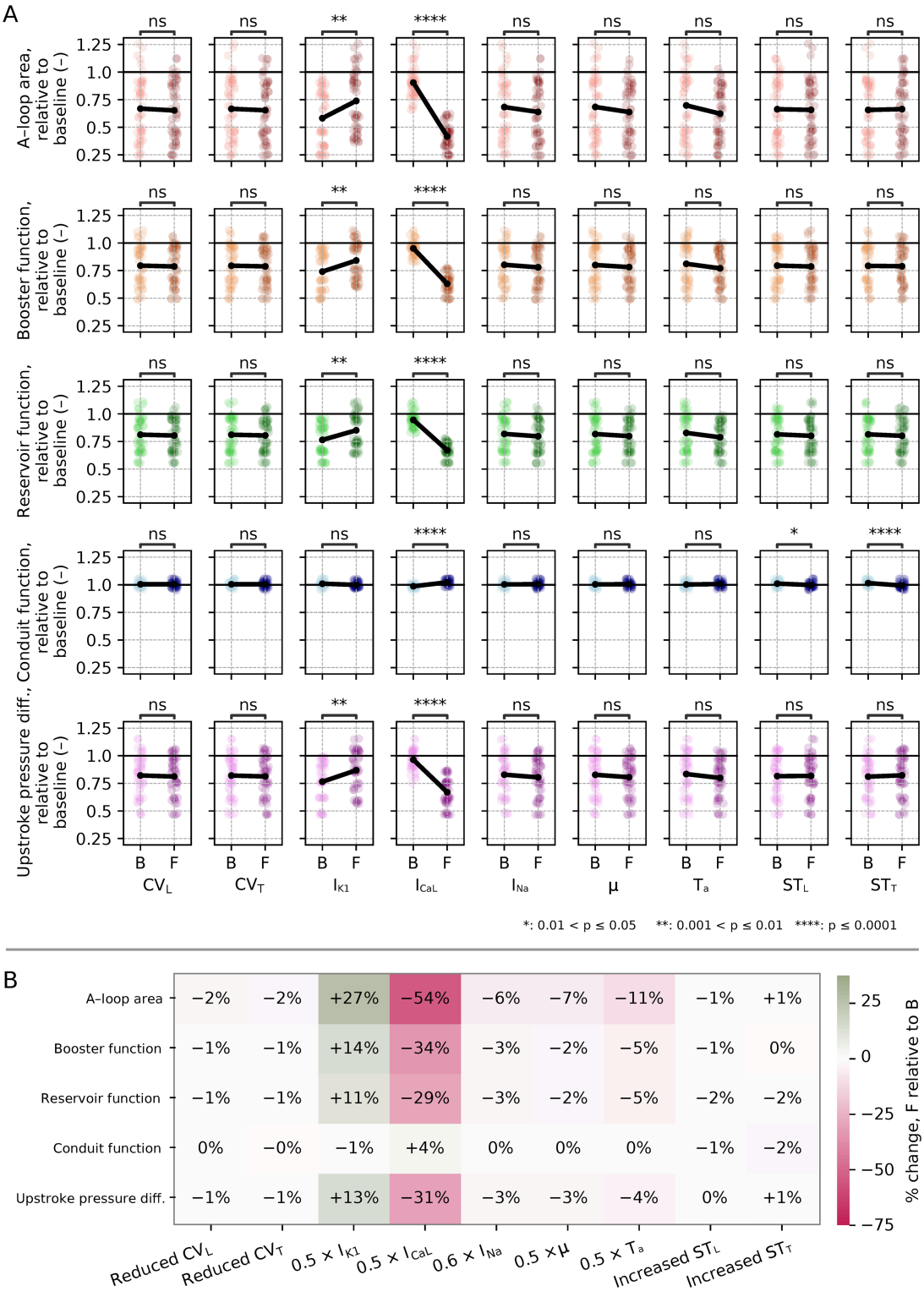

Fig 11. FFD – main effect, original fibrosis burden. (A) Main effect plots for each parameter and each metric, across all simulation combinations (Table 3) and all three patients. In each subplot, the combinations were divided into B or F groups based on whether the given parameter was set to baseline or fibrotic value. Points display values from individual simulations (i.e., all FFD combinations for all three patients), with lighter colors for the B group and darker colors for the F group. Lines show average change from B to F groups. (B) Average increase/decrease across all patients and combinations for each metric, calculated as the difference between F and B relative to B levels.

https://doi.org/10.1371/journal.pcbi.1013265.g011

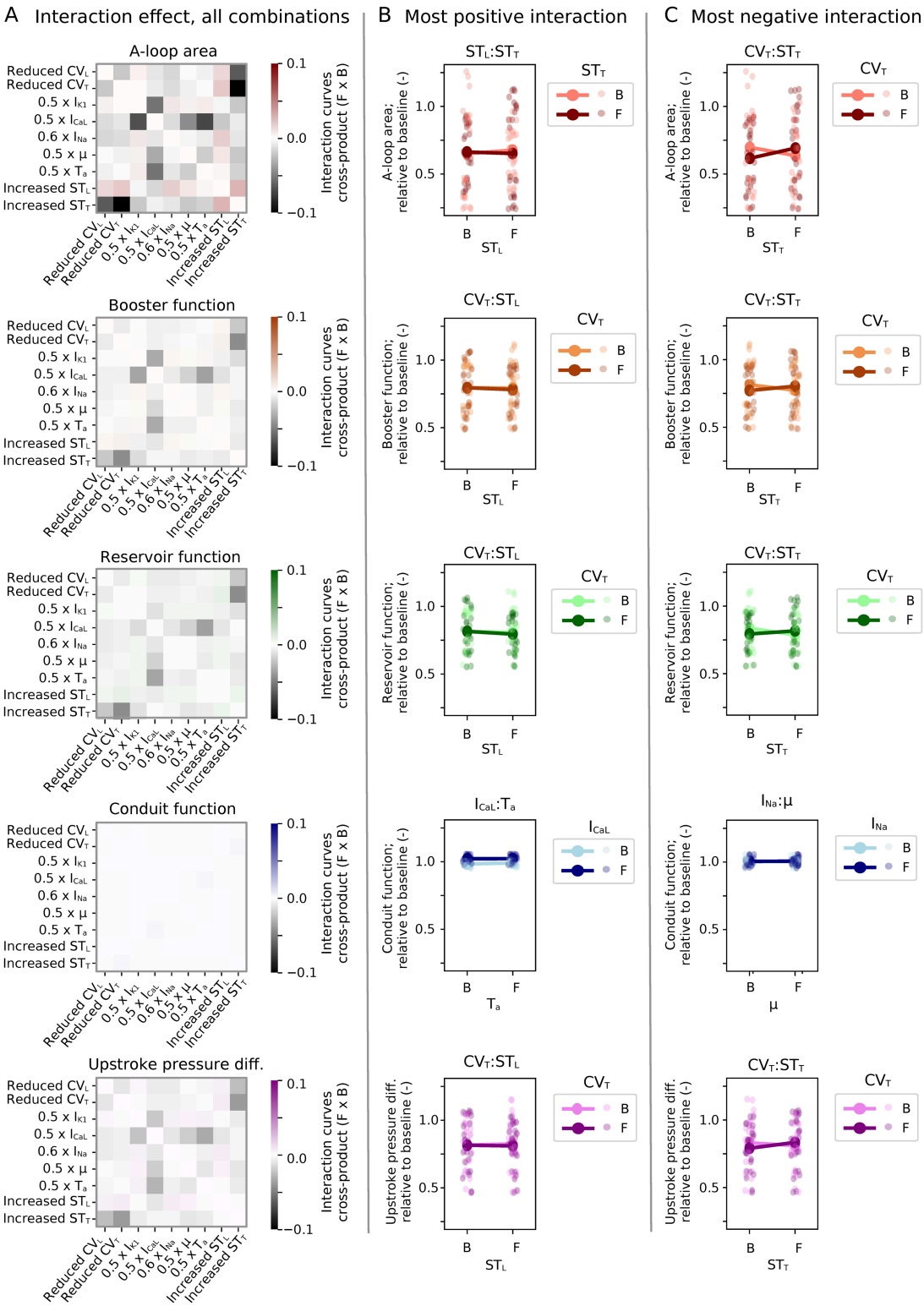

Fig 12. FFD – interactive effect, original fibrosis burden. (A) Interactive effects for each parameter pair, as calculated by Eq (6), across all FFD combinations (Table 3) and all three patients. (B–C) Interaction lines for most positive (enhancing, B) and most negative (mitigating, C) impact. Points represent values from individual simulations (i.e., all FFD combinations for all three patients), while lines display average changes within subgroups.

https://doi.org/10.1371/journal.pcbi.1013265.g012

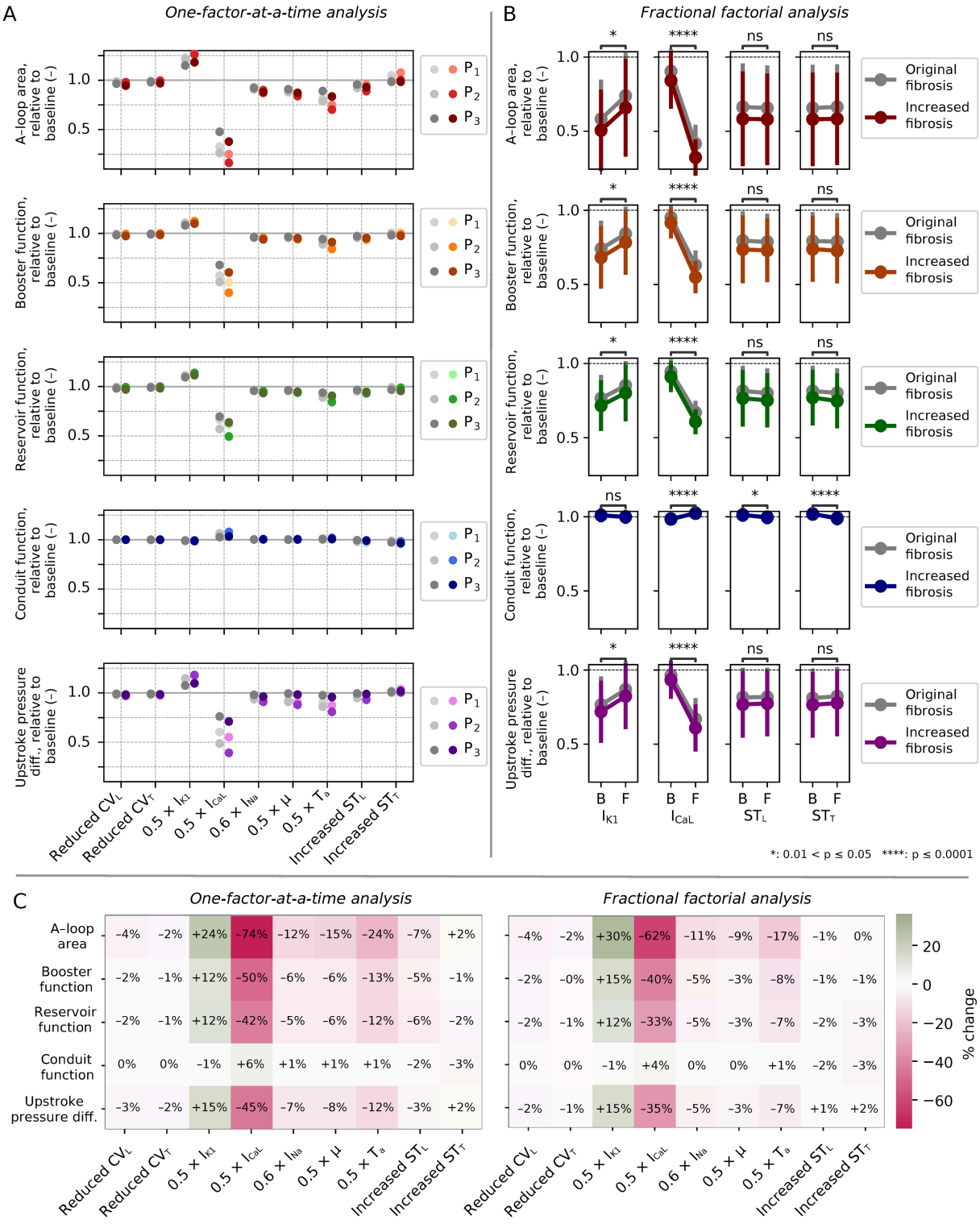

Fig 13. Impact of 50% synthetically elevated fibrosis: OFAT analysis and FFD analysis, main effect. (A) Results from the OFAT analysis for Patient 1–3 (P1–P3) patient. Original fibrosis levels are indicated by gray points on the left (the same as displayed in Fig 10) and extended fibrosis on the right. (B) FFD main effect: Error bars indicate standard deviation, and gray plots represent original fibrosis levels (based on the same underlying data as Fig 11). Comparisons for significant differences were performed for elevated fibrosis simulations. Only significant factors are displayed here, while plots for all are included in Fig F in S1 Text as described in Sect D in S1 Text. (C) Percentage impact of each parameter, averaged across all three patient cases, for OFAT (left) and the FFD (right) analyses.

https://doi.org/10.1371/journal.pcbi.1013265.g013

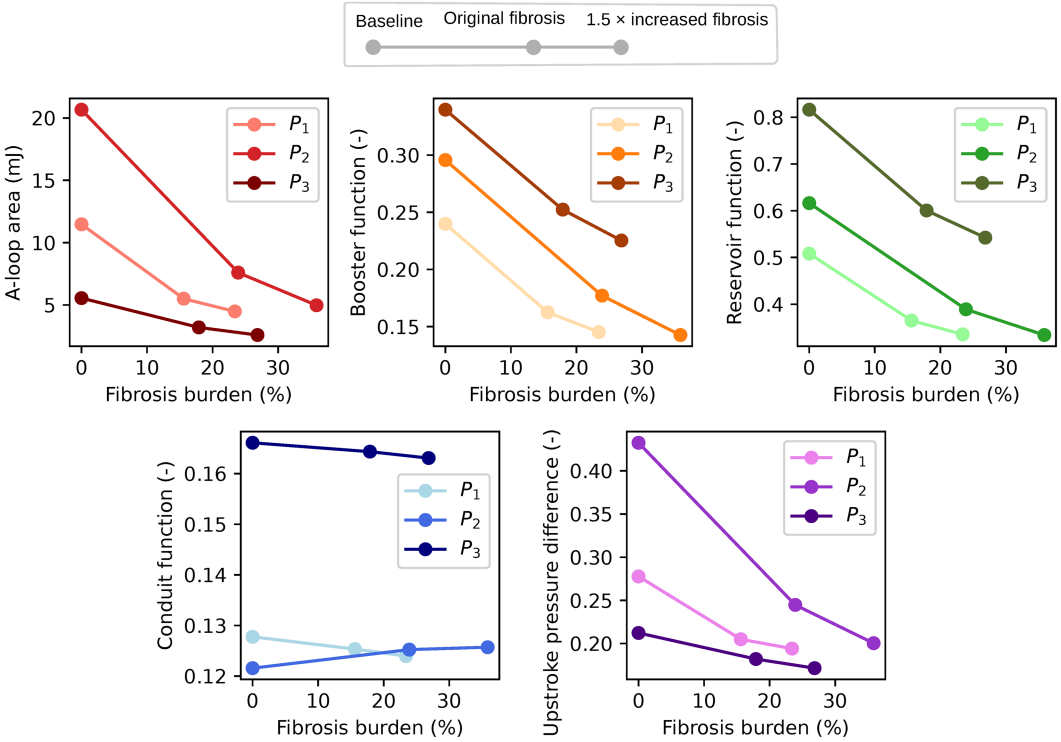

Fig 14. Absolute values of our five metrics for increasing levels of fibrosis, fully fibrotic simulation. Absolute values of A-loop area (stroke work), booster function, reservoir function, conduit function, and upstroke pressure difference for Patients 1–3 (P_1–P_3). For each patient, metrics are shown for baseline (0% fibrosis), original, and 50% synthetically increased fibrosis burdens.

https://doi.org/10.1371/journal.pcbi.1013265.g014

conductance raise intracellular calcium amplitude, whereas increasing potassium delayed rectifier conductances reduced it, consistent with our results and experimental work.

Strocchi et al. [83] performed an extensive sensitivity analysis encompassing all four cardiac chambers. Transverse atrial stiffness ($b_{t,A}$) had a stronger effect than L-type calcium channel conductance on end-systolic and end-diastolic LA volumes, whereas potassium channel conductances had little to no impact. The apparent discrepancy with our results may reflect differences in sensitivity analysis output metrics and parameterization. We observed increased stiffness to shift end-systolic and end-diastolic LA volumes but not their relative difference (i.e., booster function). Additionally, the stiffness parameter in Strocchi et al. [83] was an exponent with implied higher sensitivity. They also imposed increased stiffness throughout the atrium, whereas we applied it only to fibrotic regions.

Stiffness has also been explored in other models. Moyer et al. [17] found that fibrosis-associated increases in global stiffness reduced both systolic and diastolic function, with increased pressure and reduced volume for the latter. Meskin et al. [72] reported that higher compliance (lower stiffness) decreased pressure and increased A-loop area. Both studies advanced understanding of LA biomechanics but applied uniform stiffness changes, ignoring heterogeneity introduced by fibrotic remodeling. They also differed in material representation: our model used a reduced Holzapfel-Ogden law with a conditional term (combined with detailed fiber orientations), while the formulation used by Moyer et al. increased fiber-direction stiffness under both contraction and stretch, and Meskin et al. used silicone rubber, which is isotropic. Pericardial boundary conditions in our model may further dampen stiffness effects. We found that increased stiffness in fibrotic regions minimally reduced A-loop area, likely because changes were confined to fibrotic regions, while slightly lowering diastolic pressure, probably due to altered mitral valve flow. Gonzalo et al. [21] observed a larger systolic volume

reduction (5% vs. 2%), likely reflecting the fivefold stiffness increase in fibrotic regions, while diastolic volume remained unchanged. Physiologically, non-fibrotic regions are also probably stiffened due to interstitial fibrosis, though substantial stiffness heterogeneity remains. It seems plausible that changes in stiffness governing the largest part of the atrial body – perhaps better assessed via a median rather than mean value – will govern the relative impact on LA function.

A shift in LA volume combined with increased stiffness has been observed in clinical studies [84], although this likely included volumetric expansion. LA stiffness indices derived from clinical flow and strain measurements show predictive power [84–86], but not independently of volumetric indices. Lamy et al. [7] used invasive measurements of pressure to calculate the stiffness index and correlated it with fibrotic burden assessed by LGE. They found significant differences in LA strain metrics, but notably not in pressure. Further clinical, experimental, and computational studies are needed to better understand the relationships between LA stiffness, volume, and pressure changes.

4.2 Sensitivity analysis takeaways

We performed two types of sensitivity analysis: a simpler OFAT scheme, exploring the isolated impact of each factor, and a detailed FFD scheme, also accounting for interactive effects. We found that most of the effects could be predicted by the OFAT analysis. However, FFD analysis revealed that the impact of I_{CaL} was partially mitigated when combined with other parameter changes, while the impact of I_{K1} was amplified. In the model, these changes can be linked to shifts in equilibrium values altering action potential and calcium transient morphology (Fig 7). Physiologically, they might be considered compensatory feedback mechanisms.

Sensitivity analysis can be performed in various ways, involving many methodological choices. Advanced techniques like the Morris elementary effects method [82,87,88], Sobol indices [83,89–91], and Bayesian history matching [92,93] involve finer interval sampling, capturing non-linear behavior, interaction effects, and sensitivity regions. However, these benefits come at the cost of running more simulations. These can feasibly be carried out through model simplifications, computational optimization strategies, or surrogate models like Gaussian process emulators [54,90–93].

In our study, we sampled all relevant parameters at two levels: baseline and fibrotic. The FFD scheme presented an efficient methodology allowing us to perform our sensitivity analysis with a detailed multi-scale, multi-physics computational model, based on a manageable number of simulations. It enables direct quantification and assessment of the directionality of parameter effects, which is not provided directly through Sobol analysis nor Bayesian history matching, and only statistically approximated in the Morris elementary effects method. Finally, while OFAT is a rudimentary method that (by definition) misses all interactive effects, this attribute makes it an eminently interpretable approach.

4.3 Clinical implications

We found that fibrotic remodeling substantially impaired the cardiac function, mostly explained by impaired I_{CaL} With fibrotic area constituting between 15.6% and 23.9% (for original fibrosis burden), for the fully fibrotic simulation (with all factors set to fibrotic levels), A-loop area, booster function, reservoir function, and the difference in upstroke pressure decreased by 53%, 33%, 30%, and 28%, on average. However, with 50% increased fibrosis burden, we only saw a moderate further impairment. Our spatial analysis revealed substantial dispersive impact from the fibrotic to the non-fibrotic regions. The moderate effect could be explained by the fact that synthetically elevated fibrosis mostly covered larger areas by expansion rather than emerging in new locations. As such, these denser areas would have a less dispersive impact into non-fibrotic myocardium. This might suggest the hypothesis that scattered fibrosis distributions, as opposed to dense distributions, are more consequential for atrial dysfunction.

Two of our three patients (Patients 1 and 2, with LA volume indices 55.5 and 48.3) had enlarged LAs, with end-diastolic volumes and volume indices above normal ranges [94]. Using the Utah classification standard, Patients 1 and 3 had fibrosis burden at level II (5–20%), while Patient 2 was at level III (20–35%). Among AF patients, males have larger atria (but

not higher LA volume indices), whereas females have higher fibrosis burden [95] and larger low-voltage areas [96]. This is the opposite of what we observe for Patient 1 (female, largest LA) and Patient 2 (male, highest fibrosis burden), but not unexpected given inter-individual variability.

Several clinical studies have performed statistical analysis assessing LA strain metrics derived from clinical images. Hopman et al. [97] and Chahine et al. [98] found that reservoir, booster (contractile), and conduit strain were reduced in AF patients compared to healthy controls. In our study, we observed a decrease in booster and reservoir function, but not substantially in conduit function. Our model may not accurately capture changes in conduit function, potentially due to the use of a simplified 0D circulatory model or underestimation of traction force during LV contraction. Moreover, we only imposed changes in fibrotic regions. In reality, interstitial fibrosis in AF patients [5] raises myocardial stiffness everywhere and not only in fibrotic regions. Fibrosis levels have been found to be similar for embolic stroke of undetermined source (ESUS) and AF patients [2,99]. Bashir et al. [100] compared atrial strain metrics for ESUS patients to patients with non-cardioembolic stroke. They found that the same metrics (contractile, reservoir, and conduit) were associated with a higher risk of ESUS occurrence, and a higher risk of later AF detection.

4.4 Limitations

Most model parameter values were not patient-specific, and those that were had constraints. In calibrating patient-specific CV, we assumed healthy baseline simulation values not considering regional fibrotic changes. However, CV had low impact among the metrics considered, making this simplification reasonable. With mostly generic parameters, the models reflect general atrial characteristics, and varying patient geometries or fibrosis distributions would likely yield similar functional outcomes. The model could further be improved by personalizing parameters in the 0D circulatory model to match clinical volume and pressure-related measurements [101,102].

Beyond parameter assumptions, the model also lack several dynamic feedback mechanisms that could impact atrial function. It omits electromechanical feedback [103–106], and uses a simplified 0D circulatory model for hemodynamic feedback, which cannot fully capture fluid-structure interactions [107–109]. Fluid-structure interaction models that resolve spatial variations in endocardial pressure might be necessary to resolve secondary interactions involving regional fibrotic changes in myocardial properties. Similarly, the use of a lumped 0D model representing the impact of the other chambers, rather than a full 4-chamber model, might not accurately capture interaction between the different chambers [110]. Including at least the left ventricle could better represent the passive phase of atrial function and ventricular remodeling. However, this would greatly increase computational costs and model complexity. A potential future compromise would be to estimate patient-specific values for the CircAdapt parameters corresponding volumes of each cardiac chamber, whereas our present study used default settings for the sake of simplicity.

LAEF values in our simulations (33.70%, 38.13%, and 44.94% at baseline) were consistently lower than corresponding clinical estimates (39.24%, 51.56%, 58.2%; see Table 1). The discrepancy can be attributed to the passive part of the LAEF, which was underestimated in our model (12.78%, 12.16%, 16.61% vs. reference values of 35–40% [49, 50]), whereas active LAEFs agreed with typical normal values (23.99%, 29.57%, 33.97% vs. 30%). In the future, model improvements can be made to better represent passive function. Such improvements might also increase the sensitivity of the conduit function, which we generally found to be low.

The geometrical assumptions introduce additional limitations. We used a uniform myocardial thickness of 2 mm, although atrial wall thickness varies regionally and between patients [34], see also reported ranges in Table 1. Changes in LA volume, fibrosis burden, and wall thickness are all components of LA remodeling. Relationships between these components remain active research areas, with implications for atrial pump function and AF substrate development [34,111–113]. Additionally, myofiber architecture was specified using a rule-based algorithm. Cardiac computed tomography offers the ability to quantify regional wall thickness and patient-specific myofiber orientation [114]. Incorporating such data could enhance model accuracy and predictive value.

Our sensitivity analysis only considered a subset of all possible parameter combinations, with two levels for each parameter. There might be other influential parameters not considered in our study. Our study is also limited by the scarcity of experimental data on the relative change in each fibrosis-associated parameter. Despite these limitations, we believe the directionality of each parameter is within reasonable physiological range. Future experimental studies might refine exact parameter changes.

We only consider three patients, whereas clinical studies typically involve hundreds of patients. Combined MRI and EAM data collection is logistically challenging, while model simulations are time-consuming. Extending the analysis to a larger cohort would increase confidence in our findings and allow more granular analysis. Moreover, our analysis focuses on fibrotic regions identified by LGE, which is normalized to non-fibrotic myocardium. This approach does not capture interstitial fibrosis, which is also present among AF patients [5] and might underestimate remodeling in LGE-identified non-fibrotic regions.

4.5 Future work

This study's findings warrant future research quantifying I_{CaL}, I_{K1}, and myocardial stiffness. Clinical and experimental studies are needed to validate the results presented here, while computational studies can build on our results. Several antiarrhythmic and rate-control agents used for atrial fibrillation contain I_{K1}-blocking agents [115], while blockers of atrial-specific potassium channels (Ca^{2+}-activated K+ channels of small conductance, SK channels) have been suggested as future therapeutic drugs [116,117]. These may serve as alternatives to other medications, including but not limited to calcium channel blockers [118]. While primarily assessed in terms of arrhythmogenicity, these drugs also impact intracellular calcium and force generation. However, blocking I_{K1} may trigger ectopic activity due to increased resting membrane potential. Careful investigation is warranted regarding the balance between arrhythmic effects and benefit to atrial biomechanical function. An interesting avenue and extension of our work could be exploring the impact of rhythm control medication on atrial and ventricular function, in both sinus rhythm and subject to re-entry waves mimicking those observed in atrial and ventricular fibrillation.

Sensitivity analysis studies of the fibrotic LA could extend in several directions. Incorporation of additional parameters (e.g., other ion channels or parameters relevant to interstitial fibrosis in non-fibrotic tissue) could reveal other influential mechanisms. Wall deformation predicted by electromechanical simulations could also be integrated with spatially resolved analyses of LA flow and coagulation dynamics to assess how fibrotic remodeling affects downstream outcomes such as thrombosis risk [21,119–121]. In an extended sensitivity analysis, one could include spatiotemporal analysis of blood flow, including parameters associated to atrial morphology [122], blood rheology [123] (e.g., hematocrit and red blood cell aggregation timescale), coagulatory state, or anticoagulation regime [120]. The sensitivity analysis scheme could be extended to ventricular models or whole-heart models, considering the impact of ventricular fibrotic remodeling in comparison or in addition to atrial fibrotic remodeling.

Modeling studies with clinical data can yield mechanistically informative results. Image-based strain analysis can be combined with model-based analysis for the same individuals. Such a study would provide detailed insight into where strain analysis deviates from the model, important for model validation. Another avenue could be to combine modeling with regional analysis of fibrosis distributions [124,125], relating fibrosis burden and variations in spatial patterns to changes in LA function. Computational modeling could also compare LA function after pulmonary vein ablation [126,127], by representing veins as non-conductive, stiffer regions and possibly incorporating post-ablation LGE-MRI. Findings could be related to clinical data showing decreased LA function [71,84,128,129].

5 Conclusions

In our study, we used a computational model combined with patient-specific LA geometries to analyze the impact of nine parameters related to fibrotic remodeling. Our sensitivity analysis predicted that impairment of I_{CaL} and I_{K1} were most

consequential in terms of changes in LA function, having respectively decreased and improved effect. Future research focusing on these may greatly improve our understanding of fibrotic remodeling and its effects on atrial function. We found that reduction in I_{CaL} and I_{K1} had a dispersive effect impacting non-fibrotic tissue, and that an increase in fibrosis burden produced a comparably moderate reduction in LA function, potentially related to fibrosis density (scattered versus dense). In the future, modeling frameworks with larger cohorts could better elucidate relationships between fibrosis burden, spatial patterns, and LA function impairment. Modeling efforts could include spatiotemporal analysis of thrombogenic risk subject from fibrotic remodeling, ultimately improving risk assessment and prevention strategies.

Supporting information

S1 Text. Appendix. Supplementary text and figures providing further details of methods, underlying data, and extended results.
(PDF)

S1 Movie. Spatiotemporal electromechanical distributions, Patient 1. The movies (one for each patient) display spatiotemporal distributions of membrane voltage, intracellular calcium concentration, active tension, and fiber direction strain; for baseline, reduced I_{CaL}, reduced I_{K1}, and fully fibrotic simulations.
(M4V)

S2 Movie. Spatiotemporal electromechanical distributions, Patient 2.
(M4V)

S3 Movie. Spatiotemporal electromechanical distributions, Patient 3.
(M4V)

Author contributions

Conceptualization: Christoph M. Augustin, Patrick Boyle.

Data curation: Åshild Telle, Ahmad Kassar, Nadia Chamoun, Romanos Haykal, Tori Hensley, Yaacoub Chahine.

Formal analysis: Åshild Telle.

Funding acquisition: Juan C. del Álamo, Nazem Akoum, Christoph M. Augustin, Patrick Boyle.

Investigation: Åshild Telle.

Methodology: Åshild Telle, Christoph M. Augustin, Patrick Boyle.

Project administration: Patrick Boyle.

Resources: Nazem Akoum, Patrick Boyle.

Software: Åshild Telle, Christoph M. Augustin.

Supervision: Juan C. del Álamo, Nazem Akoum, Christoph M. Augustin, Patrick Boyle.

Validation: Alejandro Gonzalo, Oscar Flores, Juan C. del Álamo, Nazem Akoum, Christoph M. Augustin.

Visualization: Åshild Telle.

Writing – original draft: Åshild Telle.

Writing – review & editing: Åshild Telle, Ahmad Kassar, Romanos Haykal, Alejandro Gonzalo, Tori Hensley, Oscar Flores, Juan C. del Álamo, Nazem Akoum, Christoph M. Augustin, Patrick Boyle.

References

1. Pathak R, Lau DH, Mahajan R, Sanders P. Structural and functional remodeling of the left atrium: clinical and therapeutic implications for atrial fibrillation. J Atr Fibrillation. 2013;6(4):986. https://doi.org/10.4022/jafib.986 PMID: 28496919
2. Mahnkopf C, Kwon Y, Akoum N. Atrial fibrosis, ischaemic stroke and atrial fibrillation. Arrhythm Electrophysiol Rev. 2021;10(4):225–9. https://doi.org/10.15420/aer.2021.51 PMID: 35106172
3. Karakasis P, Theofilis P, Vlachakis PK, Korantzopoulos P, Patoulias D, Antoniadis AP, et al. Atrial fibrosis in atrial fibrillation: mechanistic insights, diagnostic challenges, and emerging therapeutic targets. Int J Mol Sci. 2024;26(1):209. https://doi.org/10.3390/ijms26010209 PMID: 39796066
4. Kong P, Christia P, Frangogiannis NG. The pathogenesis of cardiac fibrosis. Cell Mol Life Sci. 2014;71(4):549–74. https://doi.org/10.1007/s00018-013-1349-6 PMID: 23649149
5. Yamaguchi T. Atrial structural remodeling and atrial fibrillation substrate: a histopathological perspective. J Cardiol. 2025;85(2):47–55. https://doi.org/10.1016/j.jjcc.2024.05.007 PMID: 38810728
6. Han B, Trew ML, Zgierski-Johnston CM. Cardiac conduction velocity, remodeling and arrhythmogenesis. Cells. 2021;10(11):2923. https://doi.org/10.3390/cells10112923 PMID: 34831145
7. Lamy J, Taoutel R, Chamoun R, Akar J, Niederer S, Mojibian H, et al. Atrial fibrosis by cardiac MRI is a correlate for atrial stiffness in patients with atrial fibrillation. Int J Cardiovasc Imaging. 2024;40(1):107–17. https://doi.org/10.1007/s10554-023-02968-x PMID: 37857929
8. Neff LS, Bradshaw AD. Cross your heart? Collagen cross-links in cardiac health and disease. Cell Signal. 2021;79:109889. https://doi.org/10.1016/j.cellsig.2020.109889 PMID: 33347984
9. Li L, Zhao Q, Kong W. Extracellular matrix remodeling and cardiac fibrosis. Matrix Biol. 2018;68–69:490–506. https://doi.org/10.1016/j.matbio.2018.01.013 PMID: 29371055
10. Hamdani N, Paulus WJ. Myocardial titin and collagen in cardiac diastolic dysfunction: partners in crime. Circulation. 2013;128(1):5–8. https://doi.org/10.1161/CIRCULATIONAHA.113.003437 PMID: 23709670
11. Münch J, Abdelilah-Seyfried S. Sensing and responding of cardiomyocytes to changes of tissue stiffness in the diseased heart. Front Cell Dev Biol. 2021;9:642840. https://doi.org/10.3389/fcell.2021.642840 PMID: 33718383
12. Stroik D, Gregorich ZR, Raza F, Ge Y, Guo W. Titin: roles in cardiac function and diseases. Front Physiol. 2024;15:1385821. https://doi.org/10.3389/fphys.2024.1385821 PMID: 38660537
13. Roney CH, Bayer JD, Zahid S, Meo M, Boyle PMJ, Trayanova NA, et al. Modelling methodology of atrial fibrosis affects rotor dynamics and electrograms. Europace. 2016;18(suppl 4):iv146–55. https://doi.org/10.1093/europace/euw365 PMID: 28011842
14. Zahid S, Cochet H, Boyle PM, Schwarz EL, Whyte KN, Vigmond EJ, et al. Patient-derived models link re-entrant driver localization in atrial fibrillation to fibrosis spatial pattern. Cardiovasc Res. 2016;110(3):443–54. https://doi.org/10.1093/cvr/cvw073 PMID: 27056895
15. Bifulco SF, Scott GD, Sarairah S, Birjandian Z, Roney CH, Niederer SA, et al. Computational modeling identifies embolic stroke of undetermined source patients with potential arrhythmic substrate. Elife. 2021;10:e64213. https://doi.org/10.7554/eLife.64213 PMID: 33942719
16. Macheret F, Bifulco SF, Scott GD, Kwan KT, Chahine Y, Afroze T, et al. Comparing inducibility of re-entrant arrhythmia in patient-specific computational models to clinical atrial fibrillation phenotypes. Clinical Electrophysiology. 2023;9(10):2149–62.
17. Moyer CB, Norton PT, Ferguson JD, Holmes JW. Changes in global and regional mechanics due to atrial fibrillation: insights from a coupled finite-element and circulation model. Ann Biomed Eng. 2015;43(7):1600–13. https://doi.org/10.1007/s10439-015-1256-0 PMID: 25631205
18. Roche E, Singh M, Mendez K, Ayers B, Wang S, Takahashi A, et al. Integrating soft robotics and computational models to study left atrial hemodynamics and device testing in sinus rhythm and atrial fibrillation. Research Square [Preprint]. 2025; p. rs–3.
19. Ruz O, Vidrascu M, Chapelle D, Fernández MA. 3D-shell electromechanical modeling of the left atrium inriahalscience/hal-05044627v1. arXiv preprint 2025.
20. Paliwal N, Ali RL, Salvador M, O'Hara R, Yu R, Daimee UA, et al. Presence of left atrial fibrosis may contribute to aberrant hemodynamics and increased risk of stroke in atrial fibrillation patients. Front Physiol. 2021;12:657452. https://doi.org/10.3389/fphys.2021.657452 PMID: 34163372
21. Gonzalo A, Augustin CM, Bifulco SF, Telle Å, Chahine Y, Kassar A, et al. Multiphysics simulations reveal haemodynamic impacts of patient-derived fibrosis-related changes in left atrial tissue mechanics. J Physiol. 2024;602(24):6789–812. https://doi.org/10.1113/JP287011 PMID: 39513553
22. Dhamala J, Arevalo HJ, Sapp J, Horacek M, Wu KC, Trayanova NA, et al. Spatially adaptive multi-scale optimization for local parameter estimation in cardiac electrophysiology. IEEE Trans Med Imaging. 2017;36(9):1966–78. https://doi.org/10.1109/TMI.2017.2697820 PMID: 28459685
23. Levrero-Florencio F, Margara F, Zacur E, Bueno-Orovio A, Wang ZJ, Santiago A, et al. Sensitivity analysis of a strongly-coupled human-based electromechanical cardiac model: Effect of mechanical parameters on physiologically relevant biomarkers. Comput Methods Appl Mech Eng. 2020;361:112762. https://doi.org/10.1016/j.cma.2019.112762 PMID: 32565583
24. Srivastava JN, Anderson DA. Optimal fractional factorial plans for main effects orthogonal to two- factor interactions: 2 m series. Journal of the American Statistical Association. 1970;65(330):828. https://doi.org/10.2307/2284590
25. Box GEP, Hunter JS. The 2 k-p fractional factorial designs part I. Technometrics. 2000;42(1):28. https://doi.org/10.2307/1271430

26. Du D, Yang H, Ednie AR, Bennett ES. Statistical metamodeling and sequential design of computer experiments to model glyco-altered gating of sodium channels in cardiac myocytes. IEEE J Biomed Health Inform. 2016;20(5):1439–52. https://doi.org/10.1109/JBHI.2015.2458791 PMID: 26208370
27. Kim H, Yang H, Ednie AR, Bennett ES. Model-guided concurrent data assimilation for calibrating cardiac ion-channel kinetics. IISE Transactions on Healthcare Systems Engineering. 2023;14(2):153–66. https://doi.org/10.1080/24725579.2023.2239271
28. Lantz J, Gupta V, Henriksson L, Karlsson M, Persson A, Carlhäll C-J, et al. Impact of pulmonary venous inflow on cardiac flow simulations: comparison with in vivo 4D flow MRI. Ann Biomed Eng. 2019;47(2):413–24. https://doi.org/10.1007/s10439-018-02153-5 PMID: 30362080
29. Ashrafee A, Yashfe SMS, Khan NS, Islam MT, Azam MG, Arafat MT. Design of experiment approach to identify the dominant geometrical feature of left coronary artery influencing atherosclerosis. Biomed Phys Eng Express. 2024;10(3):10.1088/2057-1976/ad2f59. https://doi.org/10.1088/2057-1976/ad2f59 PMID: 38430572
30. Yang H, Yao B. Multi-scale simulation modeling of cardiac systems. Sensing, modeling and optimization of cardiac systems: a new generation of digital twin for heart health informatics. Springer; 2023. p. 7–38.
31. Marrouche NF, Wilber D, Hindricks G, Jais P, Akoum N, Marchlinski F, et al. Association of atrial tissue fibrosis identified by delayed enhancement MRI and atrial fibrillation catheter ablation: the DECAAF study. JAMA. 2014;311(5):498–506. https://doi.org/10.1001/jama.2014.3 PMID: 24496537
32. Marrouche NF, Greene T, Dean JM, Kholmovski EG, Boer LM, Mansour M, et al. Efficacy of LGE-MRI-guided fibrosis ablation versus conventional catheter ablation of atrial fibrillation: the DECAAF II trial: study design. J Cardiovasc Electrophysiol. 2021;32(4):916–24. https://doi.org/10.1111/jce.14957 PMID: 33600025
33. Beinart R, Abbara S, Blum A, Ferencik M, Heist K, Ruskin J, et al. Left atrial wall thickness variability measured by CT scans in patients undergoing pulmonary vein isolation. J Cardiovasc Electrophysiol. 2011;22(11):1232–6. https://doi.org/10.1111/j.1540-8167.2011.02100.x PMID: 21615817
34. Silva Cunha P, Laranjo S, Monteiro S, Almeida IG, Mendonça T, Fontes I, et al. Left atrial wall thickness estimated by cardiac CT: implications for catheter ablation of atrial fibrillation. J Clin Med. 2024;13(18):5379. https://doi.org/10.3390/jcm13185379 PMID: 39336866
35. Zappon E, Azzolin L, Gsell MA, Thaler F, Prassl AJ, Arnold R. An efficient end-to-end computational framework for the generation of ECG calibrated volumetric models of human atrial electrophysiology. arXiv preprint 2025. https://arxiv.org/abs/250203322
36. Azzolin L, Eichenlaub M, Nagel C, Nairn D, Sánchez J, Unger L, et al. AugmentA: patient-specific augmented atrial model generation tool. Comput Med Imaging Graph. 2023;108:102265. https://doi.org/10.1016/j.compmedimag.2023.102265 PMID: 37392493
37. Telle Å, Kassar A, Chamoun N, Haykal R, Gonzalo A, Hensley T. Systematic computational assessment of atrial function impairment due to fibrotic remodeling in electromechanical properties. 2025. https://doi.org/10.5061/dryad.g79cnp62q
38. Williams SE, Roney CH, Connolly A, Sim I, Whitaker J, O'Hare D, et al. OpenEP: a cross-platform electroanatomic mapping data format and analysis platform for electrophysiology research. Front Physiol. 2021;12:646023. https://doi.org/10.3389/fphys.2021.646023 PMID: 33716795
39. Augustin CM, Neic A, Liebmann M, Prassl AJ, Niederer SA, Haase G, et al. Anatomically accurate high resolution modeling of human whole heart electromechanics: a strongly scalable algebraic multigrid solver method for nonlinear deformation. J Comput Phys. 2016;305:622–46. https://doi.org/10.1016/j.jcp.2015.10.045 PMID: 26819483
40. Augustin CM, Fastl TE, Neic A, Bellini C, Whitaker J, Rajani R, et al. The impact of wall thickness and curvature on wall stress in patient-specific electromechanical models of the left atrium. Biomech Model Mechanobiol. 2020;19(3):1015–34. https://doi.org/10.1007/s10237-019-01268-5 PMID: 31802292
41. Augustin CM, Gsell MAF, Karabelas E, Willemen E, Prinzen FW, Lumens J, et al. A computationally efficient physiologically comprehensive 3D-0D closed-loop model of the heart and circulation. Comput Methods Appl Mech Eng. 2021;386:114092. https://doi.org/10.1016/j.cma.2021.114092 PMID: 34630765
42. Thiagalingam A, Reddy VY, Cury RC, Abbara S, Holmvang G, Thangaroopan M, et al. Pulmonary vein contraction: characterization of dynamic changes in pulmonary vein morphology using multiphase multislice computed tomography scanning. Heart Rhythm. 2008;5(12):1645–50. https://doi.org/10.1016/j.hrthm.2008.09.010 PMID: 19084798
43. Courtemanche M, Ramirez RJ, Nattel S. Ionic mechanisms underlying human atrial action potential properties: insights from a mathematical model. Am J Physiol. 1998;275(1):H301-21. https://doi.org/10.1152/ajpheart.1998.275.1.H301 PMID: 9688927
44. Bayer JD, Boukens BJ, Krul SPJ, Roney CH, Driessen AHG, Berger WR. Acetylcholine delays atrial activation to facilitate atrial fibrillation. Frontiers in Physiology. 2019;10.
45. Neic A, Campos FO, Prassl AJ, Niederer SA, Bishop MJ, Vigmond EJ, et al. Efficient computation of electrograms and ECGs in human whole heart simulations using a reaction-eikonal model. J Comput Phys. 2017;346:191–211. https://doi.org/10.1016/j.jcp.2017.06.020 PMID: 28819329
46. Land S, Park-Holohan S-J, Smith NP, Dos Remedios CG, Kentish JC, Niederer SA. A model of cardiac contraction based on novel measurements of tension development in human cardiomyocytes. J Mol Cell Cardiol. 2017;106:68–83. https://doi.org/10.1016/j.yjmcc.2017.03.008 PMID: 28392437
47. Land S, Niederer SA. Influence of atrial contraction dynamics on cardiac function. Int J Numer Method Biomed Eng. 2018;34(3):10.1002/cnm.2931. https://doi.org/10.1002/cnm.2931 PMID: 28990354
48. Stefanadis C, Dernellis J, Stratos C, Tsiamis E, Tsioufis C, Toutouzas K, et al. Assessment of left atrial pressure-area relation in humans by means of retrograde left atrial catheterization and echocardiographic automatic boundary detection: effects of dobutamine. J Am Coll Cardiol. 1998;31(2):426–36. https://doi.org/10.1016/s0735-1097(97)00517-2 PMID: 9462589

49. Maceira AM, Cosin-Sales J, Prasad SK, Pennell DJ. Characterization of left and right atrial function in healthy volunteers by cardiovascular magnetic resonance. J Cardiovasc Magn Reson. 2016;18(1):64. https://doi.org/10.1186/s12968-016-0284-8 PMID: 27719670

50. Truong VT, Palmer C, Wolking S, Sheets B, Young M, Ngo TNM, et al. Normal left atrial strain and strain rate using cardiac magnetic resonance feature tracking in healthy volunteers. Eur Heart J Cardiovasc Imaging. 2020;21(4):446–53. https://doi.org/10.1093/ehjci/jez157 PMID: 31504357

51. Demiray H. A note on the elasticity of soft biological tissues. J Biomech. 1972;5(3):309–11. https://doi.org/10.1016/0021-9290(72)90047-4 PMID: 4666535

52. Arts T, Delhaas T, Bovendeerd P, Verbeek X, Prinzen FW. Adaptation to mechanical load determines shape and properties of heart and circulation: the CircAdapt model. Am J Physiol Heart Circ Physiol. 2005;288(4):H1943-54. https://doi.org/10.1152/ajpheart.00444.2004 PMID: 15550528

53. Walmsley J, Arts T, Derval N, Bordachar P, Cochet H, Ploux S, et al. Fast simulation of mechanical heterogeneity in the electrically asynchronous heart using the multipatch module. PLoS Comput Biol. 2015;11(7):e1004284. https://doi.org/10.1371/journal.pcbi.1004284 PMID: 26204520

54. Strocchi M, Augustin CM, Gsell MAF, Karabelas E, Neic A, Gillette K, et al. The effect of ventricular myofibre orientation on atrial dynamics. In: Functional Imaging and Modeling of the Heart: 11th International Conference, FIMH 2021, Stanford, CA, USA, June 21–25, 2021, Proceedings. 2021. p. 659–70.

55. Plank G, Loewe A, Neic A, Augustin C, Huang Y-L, Gsell MAF, et al. The openCARP simulation environment for cardiac electrophysiology. Comput Methods Programs Biomed. 2021;208:106223. https://doi.org/10.1016/j.cmpb.2021.106223 PMID: 34171774

56. Marx L, Niestrawska JA, Gsell MAF, Caforio F, Plank G, Augustin CM. Robust and efficient fixed-point algorithm for the inverse elastostatic problem to identify myocardial passive material parameters and the unloaded reference configuration. J Comput Phys. 2022;463:111266. https://doi.org/10.1016/j.jcp.2022.111266 PMID: 35662800

57. Boyle PM, Hakim JB, Zahid S, Franceschi WH, Murphy MJ, Vigmond EJ, et al. Comparing reentrant drivers predicted by image-based computational modeling and mapped by electrocardiographic imaging in persistent atrial fibrillation. Front Physiol. 2018;9:414. https://doi.org/10.3389/fphys.2018.00414 PMID: 29725307

58. Boyle PM, Hakim JB, Zahid S, Franceschi WH, Murphy MJ, Prakosa A, et al. The fibrotic substrate in persistent atrial fibrillation patients: comparison between predictions from computational modeling and measurements from focal impulse and rotor mapping. Front Physiol. 2018;9:1151. https://doi.org/10.3389/fphys.2018.01151 PMID: 30210356

59. Boyle PM, Del Álamo JC, Akoum N. Fibrosis, atrial fibrillation and stroke: clinical updates and emerging mechanistic models. Heart. 2021;107(2):99–105. https://doi.org/10.1136/heartjnl-2020-317455 PMID: 33097562

60. Mihm MJ, Yu F, Carnes CA, Reiser PJ, McCarthy PM, Van Wagoner DR, et al. Impaired myofibrillar energetics and oxidative injury during human atrial fibrillation. Circulation. 2001;104(2):174–80. https://doi.org/10.1161/01.cir.104.2.174 PMID: 11447082

61. Eiras S, Narolska NA, van Loon RB, Boontje NM, Zaremba R, Jimenez CR, et al. Alterations in contractile protein composition and function in human atrial dilatation and atrial fibrillation. J Mol Cell Cardiol. 2006;41(3):467–77. https://doi.org/10.1016/j.yjmcc.2006.06.072 PMID: 16901501

62. Mastikhina O, Moon B-U, Williams K, Hatkar R, Gustafson D, Mourad O, et al. Human cardiac fibrosis-on-a-chip model recapitulates disease hallmarks and can serve as a platform for drug testing. Biomaterials. 2020;233:119741. https://doi.org/10.1016/j.biomaterials.2019.119741 PMID: 31927251

63. Shaw RM, Rudy Y. Ionic mechanisms of propagation in cardiac tissue. Roles of the sodium and L-type calcium currents during reduced excitability and decreased gap junction coupling. Circ Res. 1997;81(5):727–41. https://doi.org/10.1161/01.res.81.5.727 PMID: 9351447

64. Boyle PM, Franceschi WH, Constantin M, Hawks C, Desplantez T, Trayanova NA, et al. New insights on the cardiac safety factor: Unraveling the relationship between conduction velocity and robustness of propagation. J Mol Cell Cardiol. 2019;128:117–28. https://doi.org/10.1016/j.yjmcc.2019.01.010 PMID: 30677394

65. Costa CM, Hoetzl E, Rocha BM, Prassl AJ, Plank G. Automatic parameterization strategy for cardiac electrophysiology simulations. Comput Cardiol (2010). 2013;40:373–6. PMID: 24729986

66. Telle Å, Trotter JD, Cai X, Finsberg H, Kuchta M, Sundnes J, et al. A cell-based framework for modeling cardiac mechanics. Biomech Model Mechanobiol. 2023;22(2):515–39. https://doi.org/10.1007/s10237-022-01660-8 PMID: 36602715

67. Telle Å. Software for stretch experiments performed for mechanical parameter calibration. Zenodo. 2025. https://doi.org/10.5281/zenodo.15693907

68. Trutna L, Spagon P, del Castillo E, Moore T, Hartley S, Hurwitz A. NIST/SEMATECH e-Handbook of Statistical Methods. http://www.itl.nist.gov/div898/handbook/

69. Telle Å, Kassar A, Chamoun N, Haykal R, Gonzalo A, Hensley T. Software for the sensitivity analysis performed in “Systematic computational assessment of atrial function impairment due to fibrotic remodeling in electromechanical properties”. 2025.

70. Inoue K, Kawakami H, Akazawa Y, Higashi H, Higaki T, Yamaguchi O. Echocardiographic assessment of atrial function: from basic mechanics to specific cardiac diseases. J Cardiovasc Dev Dis. 2022;9(3):68. https://doi.org/10.3390/jcdd9030068 PMID: 35323616

71. Karanasos A, Tyrovolas K, Tsiachris D, Efremidis M, Kordalis A, Karmpalioti M, et al. Left atrial function post radiofrequency and cryoballoon ablation assessed by volume-pressure loops. Front Cardiovasc Med. 2022;9:830055. https://doi.org/10.3389/fcvm.2022.830055 PMID: 35355975

72. Meskin M, Starkey PA, Kaspersen AE, Ringgaard S, Sand SG, Nygaard JV, et al. Investigating the importance of left atrial compliance on fluid dynamics in a novel mock circulatory loop. Sci Rep. 2024;14(1):1864. https://doi.org/10.1038/s41598-024-52327-6 PMID: 38253772

73. Hoit BD. Evaluation of left atrial function: current status. Structural Heart. 2017;1(3–4):109–20. https://pubmed.ncbi.nlm.nih.gov/30151628/ PMID: 30151628

74. Thomas L, Marwick TH, Popescu BA, Donal E, Badano LP. Left atrial structure and function, and left ventricular diastolic dysfunction: JACC state-of-the-art review. J Am Coll Cardiol. 2019;73(15):1961–77. https://doi.org/10.1016/j.jacc.2019.01.059 PMID: 31000000

75. Charlier F, Weber M, Izak D, Harkin E, Magnus M, Lalli J. Statannotations. 2022. https://doi.org/10.5281/zenodo.7213391

76. Grandi E, Pandit SV, Voigt N, Workman AJ, Dobrev D, Jalife J, et al. Human atrial action potential and Ca2+ model: sinus rhythm and chronic atrial fibrillation. Circ Res. 2011;109(9):1055–66. https://doi.org/10.1161/CIRCRESAHA.111.253955 PMID: 21921263

77. Bers DM. Calcium fluxes involved in control of cardiac myocyte contraction. Circ Res. 2000;87(4):275–81. https://doi.org/10.1161/01.res.87.4.275 PMID: 10948060

78. Denham NC, Pearman CM, Caldwell JL, Madders GWP, Eisner DA, Trafford AW, et al. Calcium in the pathophysiology of atrial fibrillation and heart failure. Front Physiol. 2018;9:1380. https://doi.org/10.3389/fphys.2018.01380 PMID: 30337881

79. Mazzanti M, DiFrancesco D. Intracellular Ca modulates K-inward rectification in cardiac myocytes. Pflugers Arch. 1989;413(3):322–4. https://doi.org/10.1007/BF00583549 PMID: 2717377

80. Zaza A, Rocchetti M, Brioschi A, Cantadori A, Ferroni A. Dynamic Ca2+-induced inward rectification of K+ current during the ventricular action potential. Circ Res. 1998;82(9):947–56. https://doi.org/10.1161/01.res.82.9.947 PMID: 9598592

81. Fauconnier J, Lacampagne A, Rauzier J-M, Vassort G, Richard S. Ca2+-dependent reduction of IK1 in rat ventricular cells: a novel paradigm for arrhythmia in heart failure?. Cardiovasc Res. 2005;68(2):204–12. https://doi.org/10.1016/j.cardiores.2005.05.024 PMID: 16083867

82. Hurtado DE, Castro S, Madrid P. Uncertainty quantification of 2 models of cardiac electromechanics. Int J Numer Method Biomed Eng. 2017;33(12):10.1002/cnm.2894. https://doi.org/10.1002/cnm.2894 PMID: 28474497

83. Strocchi M, Longobardi S, Augustin CM, Gsell MAF, Petras A, Rinaldi CA, et al. Cell to whole organ global sensitivity analysis on a four-chamber heart electromechanics model using Gaussian processes emulators. PLoS Comput Biol. 2023;19(6):e1011257. https://doi.org/10.1371/journal.pcbi.1011257 PMID: 37363928

84. Khurram IM, Maqbool F, Berger RD, Marine JE, Spragg DD, Ashikaga H, et al. Association between left atrial stiffness index and atrial fibrillation recurrence in patients undergoing left atrial ablation. Circ Arrhythm Electrophysiol. 2016;9(3):e003163. https://doi.org/10.1161/CIRCEP.115.003163 PMID: 26966287

85. Kishima H, Mine T, Fukuhara E, Ashida K, Ishihara M. The association between left atrial stiffness and low-voltage areas of left atrium in patients with atrial fibrillation. Heart Vessels. 2019;34(11):1830–8. https://doi.org/10.1007/s00380-019-01423-z PMID: 31049675

86. Kim D, Seo JH, Choi KH, Lee SH, Choi JO, Jeon ES, et al. Prognostic implications of left atrial stiffness index in heart failure patients with preserved ejection fraction. Cardiovascular Imaging. 2023;16(4):435–45. https://doi.org/10.1016/j.jcmg.2022.11.002 PMID: 36752431

87. Le Rolle V, Galli E, Danan D, El Houari K, Hubert A, Donal E, et al. Sensitivity analysis of a left ventricle model in the context of intraventricular dyssynchrony. Acta Biotheor. 2020;68(1):45–59. https://doi.org/10.1007/s10441-019-09362-y PMID: 31506833

88. Taconné M, Owashi KP, Galli E, Duchenne J, Hubert A, Donal E, et al. Model-based analysis of myocardial strains in left bundle branch block. Front Appl Math Stat. 2022;8. https://doi.org/10.3389/fams.2022.833003

89. Pathmanathan P, Cordeiro JM, Gray RA. Comprehensive uncertainty quantification and sensitivity analysis for cardiac action potential models. Front Physiol. 2019;10:721. https://doi.org/10.3389/fphys.2019.00721 PMID: 31297060

90. Karabelas E, Longobardi S, Fuchsberger J, Razeghi O, Rodero C, Strocchi M, et al. Global sensitivity analysis of four chamber heart hemodynamics using surrogate models. IEEE Trans Biomed Eng. 2022;69(10):3216–23. https://doi.org/10.1109/TBME.2022.3163428 PMID: 35353691

91. Lazarus A, Dalton D, Husmeier D, Gao H. Sensitivity analysis and inverse uncertainty quantification for the left ventricular passive mechanics. Biomech Model Mechanobiol. 2022;21(3):953–82. https://doi.org/10.1007/s10237-022-01571-8 PMID: 35377030

92. Longobardi S, Lewalle A, Coveney S, Sjaastad I, Espe EKS, Louch WE, et al. Predicting left ventricular contractile function via Gaussian process emulation in aortic-banded rats. Philos Trans A Math Phys Eng Sci. 2020;378(2173):20190334. https://doi.org/10.1098/rsta.2019.0334 PMID: 32448071

93. Jones CE, Oomen PJA. Synergistic biophysics and machine learning modeling to rapidly predict cardiac growth probability. Comput Biol Med. 2025;184:109323. https://doi.org/10.1016/j.compbiomed.2024.109323 PMID: 39515269

94. Kawel-Boehm N, Hetzel SJ, Ambale-Venkatesh B, Captur G, Francois CJ, Jerosch-Herold M, et al. Reference ranges ("normal values") for cardiovascular magnetic resonance (CMR) in adults and children: 2020 update. J Cardiovasc Magn Reson. 2020;22(1):87. https://doi.org/10.1186/s12968-020-00683-3 PMID: 33308262

95. Akoum N, Mahnkopf C, Kholmovski EG, Brachmann J, Marrouche NF. Age and sex differences in atrial fibrosis among patients with atrial fibrillation. Europace. 2018;20(7):1086–92. https://doi.org/10.1093/europace/eux260 PMID: 29016990

96. Van Leuven O, Bergonti M, Spera FR, Ferrero TG, Nsahlai M, Bilotta G, et al. Gender-related differences in atrial substrate in patients with atrial fibrillation. Am J Cardiol. 2023;203:451–8. https://doi.org/10.1016/j.amjcard.2023.06.095 PMID: 37540903

97. Hopman LHGA, Mulder MJ, van der Laan AM, Demirkiran A, Bhagirath P, van Rossum AC, et al. Impaired left atrial reservoir and conduit strain in patients with atrial fibrillation and extensive left atrial fibrosis. J Cardiovasc Magn Reson. 2021;23(1):131. https://doi.org/10.1186/s12968-021-00820-6 PMID: 34758820

98. Chahine Y, Chamoun N, Kassar A, Bockus L, Macheret F, Akoum N. Atrial fibrillation substrate and impaired left atrial function: a cardiac MRI study. Europace. 2024;26(11):euae258. https://doi.org/10.1093/europace/euae258 PMID: 39523754

99. Koh JH, Lim LKE, Tan YK, Goh C, Teo YH, Ho JSY, et al. Assessment of left atrial fibrosis by cardiac magnetic resonance imaging in ischemic stroke patients without atrial fibrillation: a systematic review and meta-analysis. J Am Heart Assoc. 2024;13(17):e033059. https://doi.org/10.1161/JAHA.123.033059 PMID: 39190571

100. Bashir Z, Chen EW, Wang S, Shu L, Goldstein ED, Rana M, et al. Left atrial strain, embolic stroke of undetermined source, and atrial fibrillation detection. Echocardiography. 2024;41(1):e15738. https://doi.org/10.1111/echo.15738 PMID: 38284672

101. Casas B, Lantz J, Viola F, Cedersund G, Bolger AF, Carlhäll CJ. Bridging the gap between measurements and modelling: a cardiovascular functional avatar. Scientific Reports. 2017;7(1):6214. https://doi.org/10.1038/s41598-017-06339-0 PMID: 28740184

102. Shi L, Chen IY, Vedula V. Personalized multiscale modeling of left atrial mechanics and blood flow. Sci Rep. 2026; 448(A). https://doi.org/10.1016/j.cma.2025.118412

103. Pfeiffer ER, Tangney JR, Omens JH, McCulloch AD. Biomechanics of cardiac electromechanical coupling and mechanoelectric feedback. J Biomech Eng. 2014;136(2):021007. https://doi.org/10.1115/1.4026221 PMID: 24337452

104. Orini M, Nanda A, Yates M, Di Salvo C, Roberts N, Lambiase PD, et al. Mechano-electrical feedback in the clinical setting: current perspectives. Prog Biophys Mol Biol. 2017;130(Pt B):365–75. https://doi.org/10.1016/j.pbiomolbio.2017.06.001 PMID: 28587763

105. Satriano A, Vigmond EJ, Schwartzman DS, Di Martino ES. Mechano-electric finite element model of the left atrium. Computers in Biology and Medicine. 2018;96:24–31. https://doi.org/10.1016/j.compbiomed.2018.02.010 PMID: 29529527

106. Gerach T, Loewe A. Differential effects of mechano-electric feedback mechanisms on whole-heart activation, repolarization, and tension. J Physiol. 2024;602(18):4605–24. https://doi.org/10.1113/JP285022 PMID: 38185911

107. Feng L, Gao H, Griffith B, Niederer S, Luo X. Analysis of a coupled fluid-structure interaction model of the left atrium and mitral valve. Int J Numer Method Biomed Eng. 2019;35(11):e3254. https://doi.org/10.1002/cnm.3254 PMID: 31454470

108. Viola F, Meschini V, Verzicco R. Fluid–Structure-Electrophysiology interaction (FSEI) in the left-heart: a multi-way coupled computational model. European Journal of Mechanics - B/Fluids. 2020;79:212–32. https://doi.org/10.1016/j.euromechflu.2019.09.006

109. Syed F, Khan S, Toma M. Modeling dynamics of the cardiovascular system using fluid-structure interaction methods. Biology (Basel). 2023;12(7):1026. https://doi.org/10.3390/biology12071026 PMID: 37508455

110. Brown AL, Liu J, Ennis DB, Marsden AL. Cardiac mechanics modeling: recent developments and current challenges. arXiv preprint 2025. https://arxiv.org/abs/250907971

111. Olsen FJ, Bertelsen L, Vejlstrup N, Diederichsen SZ, Bjerregaard CL, Graff C, et al. Association between four-dimensional echocardiographic left atrial measures and left atrial fibrosis assessed by left atrial late gadolinium enhancement. Eur Heart J Cardiovasc Imaging. 2022;24(1):152–61. https://doi.org/10.1093/ehjci/jeab275 PMID: 34964463

112. Li L, Li L, Yang D, Nong S, Luo C, Gui C. Analysis of the thickness characteristics of the left atrial posterior wall and its correlation with the low and no voltage areas of the left atrial posterior wall in patients with atrial fibrillation. J Cardiothorac Surg. 2024;19(1):187. https://doi.org/10.1186/s13019-024-02658-2 PMID: 38582871

113. Liu W, Li S, Dou L, Hu C, Han B. Identification of left atrial wall thickness in substrate mapping of atrial fibrillation. Front Cardiovasc Med. 2025;12:1592532. https://doi.org/10.3389/fcvm.2025.1592532 PMID: 40636832

114. Bodagh N, Williams MC, Vickneson K, Gharaviri A, Niederer S, Williams SE. State of the art paper: cardiac computed tomography of the left atrium in atrial fibrillation. J Cardiovasc Comput Tomogr. 2023;17(3):166–76. https://doi.org/10.1016/j.jcct.2023.03.002 PMID: 36966040

115. Reilly L, Eckhardt LL. Cardiac potassium inward rectifier Kir2: Review of structure, regulation, pharmacology, and arrhythmogenesis. Heart Rhythm. 2021;18(8):1423–34. https://doi.org/10.1016/j.hrthm.2021.04.008 PMID: 33857643

116. Ravens U, Odening KE. Atrial fibrillation: therapeutic potential of atrial K+ channel blockers. Pharmacol Ther. 2017;176:13–21. https://doi.org/10.1016/j.pharmthera.2016.10.003 PMID: 27742566

117. Qi M-M, Qian L-L, Wang R-X. Modulation of SK channels: insight into therapeutics of atrial fibrillation. Heart Lung Circ. 2021;30(8):1130–9. https://doi.org/10.1016/j.hlc.2021.01.009 PMID: 33642173

118. Scheuermeyer FX, Grafstein E, Stenstrom R, Christenson J, Heslop C, Heilbron B, et al. Safety and efficiency of calcium channel blockers versus beta-blockers for rate control in patients with atrial fibrillation and no acute underlying medical illness. Acad Emerg Med. 2013;20(3):222–30. https://doi.org/10.1111/acem.12091 PMID: 23517253

119. Kjeldsberg HA, Albors C, Mill J, Medel DV, Camara O, Sundnes J, et al. Impact of left atrial wall motion assumptions in fluid simulations on proposed predictors of thrombus formation. Int J Numer Method Biomed Eng. 2024;40(6):e3825. https://doi.org/10.1002/cnm.3825 PMID: 38629309

120. Guerrero-Hurtado M, García-Villalba M, Gonzalo A, Durán E, Martinez-Legazpi P, Ávila P, et al. Hemodynamics affects factor XI/XII anticoagulation efficacy in patient-derived left atrial models. Comput Methods Programs Biomed. 2025;267:108761. https://doi.org/10.1016/j.cmpb.2025.108761 PMID: 40318574

121. Qureshi A, Melidoro P, Balmus M, Lip GYH, Nordsletten DA, Williams SE, et al. MRI-based modelling of left atrial flow and coagulation to predict risk of thrombogenesis in atrial fibrillation. Med Image Anal. 2025;101:103475. https://doi.org/10.1016/j.media.2025.103475 PMID: 39864279

122. Di Biase L, Santangeli P, Anselmino M, Mohanty P, Salvetti I, Gili S, et al. Does the left atrial appendage morphology correlate with the risk of stroke in patients with atrial fibrillation? Results from a multicenter study. J Am Coll Cardiol. 2012;60(6):531–8. https://doi.org/10.1016/j.jacc.2012.04.032 PMID: 22858289

123. Gonzalo A, García-Villalba M, Rossini L, Durán E, Vigneault D, Martínez-Legazpi P, et al. Non-Newtonian blood rheology impacts left atrial stasis in patient-specific simulations. Int J Numer Method Biomed Eng. 2022;38(6):e3597. https://doi.org/10.1002/cnm.3597 PMID: 35344280

124. Assaf A, Mekhael M, Noujaim C, Chouman N, Younes H, Feng H, et al. Effect of fibrosis regionality on atrial fibrillation recurrence: insights from DECAAF II. Europace. 2023;25(9):euad199. https://doi.org/10.1093/europace/euad199 PMID: 37428891

125. Benito EM, Cabanelas N, Nuñez-Garcia M, Alarcón F, Figueras I Ventura RM, Soto-Iglesias D, et al. Preferential regional distribution of atrial fibrosis in posterior wall around left inferior pulmonary vein as identified by late gadolinium enhancement cardiac magnetic resonance in patients with atrial fibrillation. Europace. 2018;20(12):1959–65. https://doi.org/10.1093/europace/euy095 PMID: 29860416

126. Phung T-KN, Moyer CB, Norton PT, Ferguson JD, Holmes JW. Effect of ablation pattern on mechanical function in the atrium. Pacing Clin Electrophysiol. 2017;40(6):648–54. https://doi.org/10.1111/pace.13086 PMID: 28370137

127. Gerach T, Schuler S, Wachter A, Loewe A. The impact of standard ablation strategies for atrial fibrillation on cardiovascular performance in a Four-Chamber heart model. Cardiovasc Eng Technol. 2023;14(2):296–314. https://doi.org/10.1007/s13239-022-00651-1 PMID: 36652165

128. Kassa KI, Nagy Z, Simkovits D, Kis Z, Ferenci T, Som Z, et al. Evaluation of isolation area, myocardial injury and left atrial function following high-power short-duration radiofrequency or second-generation cryoballoon ablation for atrial fibrillation. J Cardiovasc Dev Dis. 2022;9(10):327. https://doi.org/10.3390/jcdd9100327 PMID: 36286279

129. Liu Y, Liu Q, Yang Y, Zhang C, Yin H, Wu J, et al. Effect of radiofrequency catheter ablation on left atrial structure and function in patients with different types of atrial fibrillation. Sci Rep. 2022;12(1):9511. https://doi.org/10.1038/s41598-022-13725-w PMID: 35681013